Finestructure and microstructure in the North Atlantic Current

by Raymond W. Schmitt[1] and Daniel T. Georgi[1,2]

ABSTRACT

The relationship between intrusive finestructure and optical microstructure was studied by simultaneous CTD Tow-yos and deployments of the shadowgraph profiler SCIMP. Strong thermohaline intrusions, 5 to 50 m thick, were tracked laterally for 5 to 10 km in the front associated with the North Atlantic Current. Some of the intrusions showed significant cross-isopycnal slopes, consistent with the hypothesis that double-diffusion is causing the intrusions to cross density surfaces. The SCIMP shadowgraphs displayed clear images of salt fingers at the lower boundaries of warm salty intrusions, confirming that double-diffusion is an active mixing process in frontal interleaving zones. In addition, significant correlations of the SCIMP optical microstructure with temperature, salinity and velocity finestructure were found. Mixing activity was more likely to occur when the density ratio ($R\rho = \alpha T_z/\beta S_z$) was near one or when the Richardson number was low. These correlations show that double-diffusion was more common than shear instability in the frontal interleaving zone. In contrast, a SCIMP dive in mid-gyre showed much less activity, no interleaving, and few sites with $R\rho$ near one. Thus shear instability may account for most of the weak mixing in those mid-gyre regions where the mean T-S profiles do not favor strong double-diffusion activity. The scales of the frontal intrusions are found to be consistent with the double-diffusive generation model of Toole and Georgi (1981). Application of the Joyce (1977) lateral mixing model suggests that intrusions are a significant cross-frontal mixing mechanism.

1. Introduction

One of the issues of considerable interest in the study of ocean fine- and microstructure is the role that double-diffusive mixing may play in the behavior of the thermohaline intrusions observed at fronts. Horne (1978), Joyce *et al.* (1978) and Gregg (1980) have used closely spaced CTD profiles to map the lateral extent of 5 to 50 m-thick intrusions. These authors found that some intrusions cross density surfaces as they propagate laterally. It was suggested that double-diffusive mixing is the most likely cause of such behavior, since both salt fingers and the diffusive instability are most intense when temperature and salinity are nearly compensating in density. Experiments (Turner, 1978; Ruddick and Turner, 1979) show that the fluxes due to salt fingers dominate, causing warm-salty intrusions to lose more salt

1. Woods Hole Oceanographic Institution, Woods Hole, Massachusetts, 02543, U.S.A.
2. Present address: Exxon Production Research, P.O. Box 2189, Houston, Texas, 77001, U.S.A.

than heat and rise across density surfaces, and cold-fresh intrusions to sink. Stern (1967) predicted these effects, suggesting that the enhanced vertical mixing caused by the intrusions could be an important lateral mixing mechanism and an effective process for maintaining the tightness of the mean *T-S* relationship. That is, double-diffusion causes an intrusion to continue to cross density surfaces until it reaches a surface with the same *T-S* characteristics.

Observations by Williams (1981) have indicated the presence of double-diffusive mixing events in association with temperature and salinity inversions in the Gulf Stream. In this report, we will describe our attempt to do both the lateral mapping of the intrusions and identification of the types of mixing events by simultaneously performing a CTD Tow-yo and deploying the Williams profiler SCIMP (Self-Contained Imaging Micro-Profiler). We feel that we have successfully identified active double-diffusive mixing in association with intrusive features having significant cross-isopycnal tilts in the front associated with the North Atlantic Current. In addition, the statistical incidence of microstructure activity with respect to the observed density ratios and Richardson numbers measured by SCIMP has been examined. We find that mixing events are more likely to occur when the density ratio is close to one, suggestive of double-diffusive instabilities, and more likely to occur when the Richardson number is low, suggesting shear instability. These correlations indicate that double-diffusion is the dominant mixing mechanism in the frontal intrusions, while shear instability may do more of the mixing in weakly active mid-gyre regions.

Our work was part of a hydrographic section from the Azores to the Flemish Cap, a topographic feature east of the Grand Banks. The background hydrography and the basic data collected by SCIMP are described in Section 2. In Section 3, we present the results of the combined Tow-yo and SCIMP surveys. Section 4 describes the study of the statistical correlation of mixing events with Richardson numbers and density ratio, and in Section 5 our observations are summarized and an attempt is made to evaluate the role of intrusions in lateral mixing.

2. Background hydrography and SCIMP data

In order to study the relationship between lateral intrusions and double-diffusive mixing, we chose to perform our experiment in the strong front associated with the North Atlantic Current, in an area east of the Grand Banks. Finestructure in the front has a large amplitude, making it easier to track features laterally and assuring a strong signal level for microstructure observations. We participated in Cruise 78, Leg 5, of the R/V *Oceanus*, a hydrographic survey which included a section from the Azores to the Flemish Cap, performed in April, 1980. Figure 1 shows the ship's track and CTD station locations and the positions of the four SCIMP dives. The pattern of mean April surface isotherms (after Robinson *et al.*,

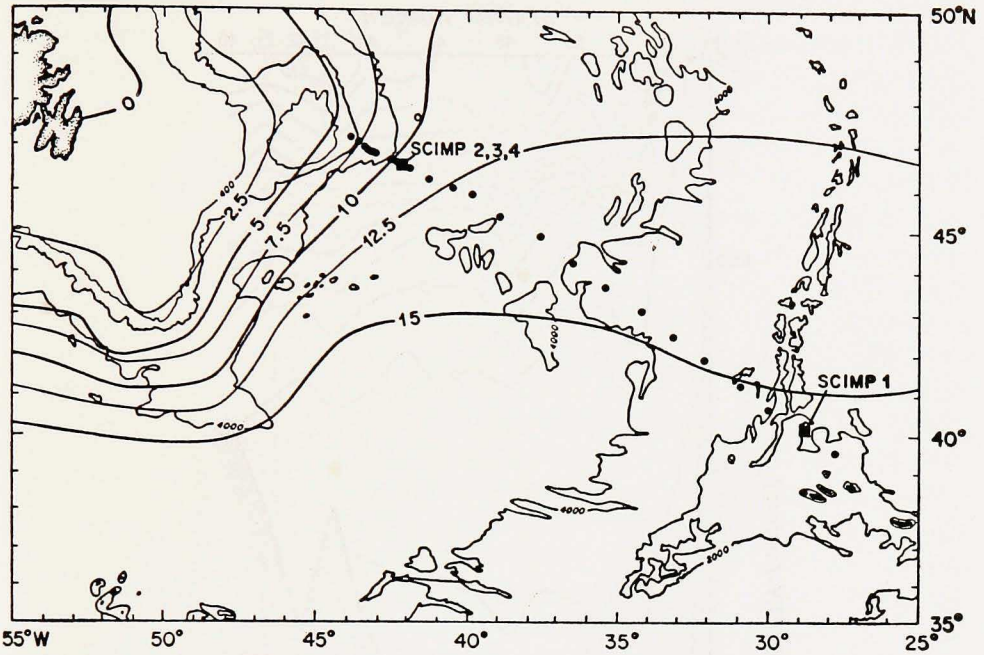

Figure 1. CTD station locations and positions of the four SCIMP dives. The mean pattern of surface isotherms for April is shown (after Robinson *et al.*, 1979). The 4000 m, 2000 m and 400 m isobaths are also shown.

1979) is also shown. Figure 2a is a potential temperature section constructed from the CTD data. The North Atlantic Current is clearly indicated by the steeply sloping isotherms at the northwestern end of the section. The front is equally obvious in the salinity section; Figure 2b reveals the warm-salty, cold-fresh contrast required for the generation of intrusions. Further details of the overall hydrography of this section and the characteristics of the finestructure sampled by the CTD will be discussed in Georgi and Schmitt (1982). The first dive with the profiler SCIMP was made after Station 41, near the beginning of the section, and three additional dives were made in the front.

SCIMP, described by Williams (1975), is a freely sinking platform carrying an internally recording Brown/WHOI CTD, an optical shadowgraph system, acoustic current meters to sense the two components of horizontal velocity relative to the vehicle, a variable buoyancy control unit, weight release mechanisms, and an acoustic telemetry link. The optical system projects a parallel beam of light through the water over an 80 cm horizontal path and focuses the image onto a ground glass screen. The resulting shadowgraph images reveal the shape and intensity of the second spatial derivative of the index of refraction in the sampled volume (Wil-

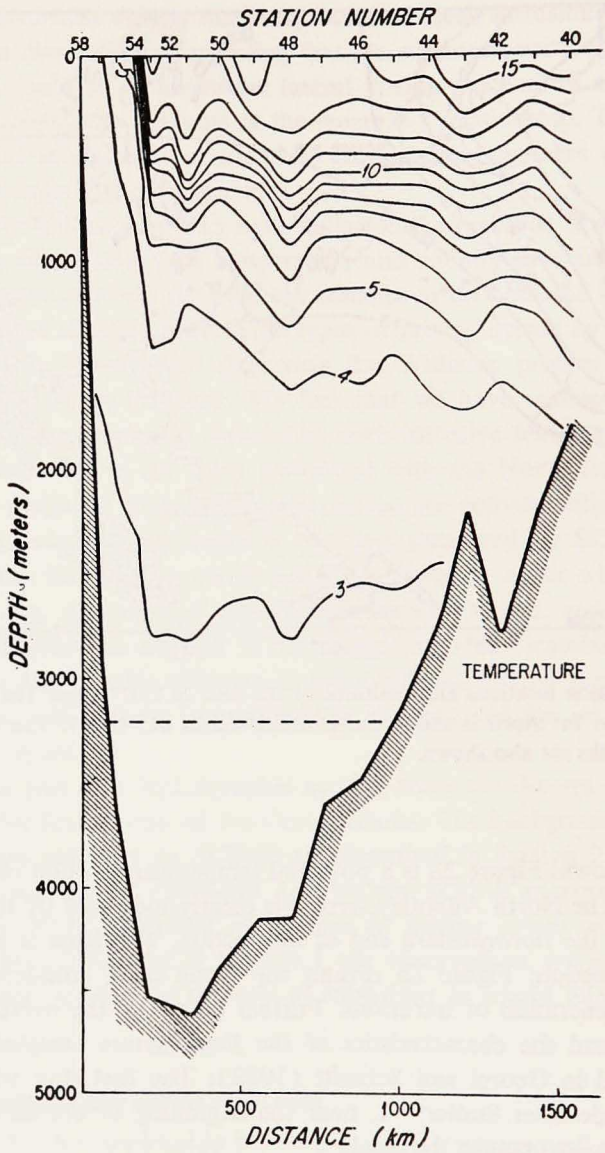

Figure 2a. Potential temperature section contoured from the CTD data. The North Atlantic Current is apparent at the strong front between stations 53 and 54.

liams, 1975). The instrument sinks at a rate between 11 and 15 cm/s; the images are photographed on super-8 mm movie film at a rate near one Hz. Since the diameter of the horizontal cylinder sampled by the system is 13.8 cm, a nearly continuous shadowgraph record of the water column is obtained. Kodak 4-X (ASA = 320) black-and-white film was used in 50 foot cartridges. This limited

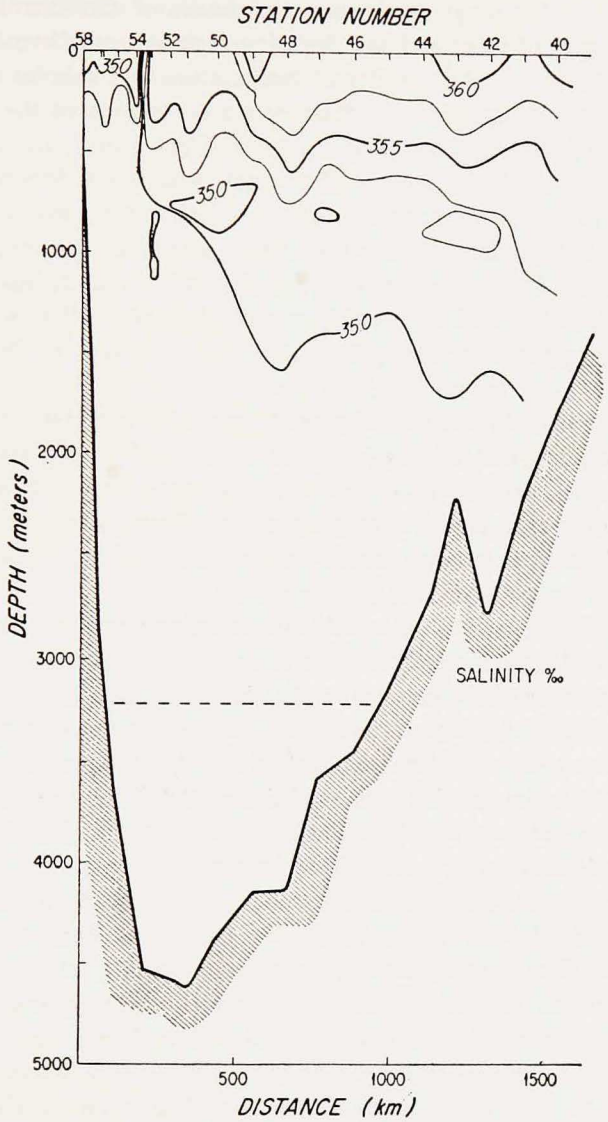

Figure 2b. The salinity section. The front has the warm-salty, cold-fresh contrast necessary to form intrusions.

the depth interval which could be logged to about 500 m. However, the enhanced sensitivity of this film more than compensated for the limited coverage; poor image quality has previously degraded the performance of this expanded beam system.

Each image is partially obscured by the shadows of a small convex mirror and its supports which are required to expand the 2.5 cm diameter beam to 13.8 cm.

Plate 1 is a composite diagram showing the details of the mirror structure and sample photographs of quiet and salt fingering regions from Dive 2, taken in the front, along with the vertical profiles of temperature and salinity. To the left of each image is a record number which permits a correlation of the optical images with the CTD and velocity data. The images of Plate 1 are particularly good examples of the vertically-banded structure characteristic of salt fingers. These fingers were observed at the lower boundary of the strong warm-salty intrusion at 190 decibars, they will be discussed more fully later. Additional examples of both mixing and non-mixing images from Dive 2 are shown in Plate 2; images with structure oriented vertically and horizontally were obtained, as well as some with structure which was apparently isotropic in the view obtained by the shadowgraph system.

Most of the frames in the film displayed very little contrast; this is consistent with previous reports that mixing is a rare event in the main thermocline. The presence of contrast on the film can be safely associated with mixing activity, since the system is only sensitive to property gradients on centimeter scales and smaller. Such short-scale features would decay diffusively in a few minutes, suggesting an active or very recent stirring process.

In order to quantify at least the incidence of mixing activity, the film for each dive was reviewed and those frames recording activity were given a subjective grade on the intensity of the contrast on the image with a 0-9 scale (9 indicating the highest contrast). A judgment was also made as to the dominant orientation of the image; using the classifications vertical (= 1), horizontal (= 2) and isotropic (= 3). The film grading was carried out "blind," prior to the analysis of the CTD data, to make the classifications as objective as possible. Williams (1975, 1981) provides further examples of SCIMP imagery.

The CTD and velocity data were recorded at 5 Hz, giving a sample every 2-3 cm in the vertical. Unfortunately, during this cruise there was an electrical noise problem which affected the pressure, temperature and conductivity data at the 1 Hz acoustic pinger rate. However, the noise was extremely regular and the affected points were easily flagged and removed with a simple algorithm. The missing data were then replaced with a linear interpolation between the adjacent good data. A symmetric Butterworth filter was then applied to all variables, with a half power point at 0.156 Hz, corresponding to vertical scales of 70 to 96 cm at the 11 to 15 cm/s fall rate of the instrument. A lag correction was then applied to the temperature, salinities computed, and the data decimated at every eighth point. The lag correction was chosen by minimizing the number of loops in the *T-S* diagrams from the frontal stations. The decimation rate resulted in data spaced at 17-23 cm intervals in the vertical. No water samples are collected by SCIMP, so we relied on the pre- and post-cruise calibrations, which agreed with each other to within 0.001°C and 0.002 mmhos/cm. Good agreement was found

between SCIMP salinities and those from nearby CTD casts.

The two components of horizontal velocity, U perpendicular to the optical path, and V parallel to the optical path, were filtered and decimated in the same way as the CTD data. The magnetic compass on SCIMP malfunctioned so the velocities could not be resolved into earth-based coordinates. Hendricks and Rodenbusch (1981) have developed a linear transfer function that can be used to correct the spectrum of shears measured by SCIMP. Evans (1979) has used a nonlinear model of the response of a similar free-fall vehicle to reconstruct the actual velocity profile. Given the complex geometry of SCIMP, such a model would be difficult to devise and would remain unverifiable without independent tracking information. Thus, we have treated the SCIMP velocity data as simply a bandpass of the true velocity, resolving features with vertical scales of 1 to 10 m.

Our first SCIMP dive was made after Station 41. Temperature and salinity decreased monotonically with depth in the upper 500 m covered by the SCIMP dive; there is little evidence of intrusive finestructure except on very small scales. Figure 3a contains profiles of T, S, σ_θ and mixing intensity (subjectively graded from the shadowgraph films). The term "mixing" is appropriate since the optical system is sensitive only to small-scale gradients where molecular diffusion becomes of direct importance. As can be seen in the profile of mixing intensity, very little activity was observed in this dive. Less than 2% of the frames displayed any notable contrast. This low incidence of mixing is consistent with other work (Gregg, 1977) finding that microstructure activity is weak in mid-gyre regions. The overall T-S gradients are in the correct sense for salt fingering and some weak 'sheets and layers' type steppiness is apparent, especially between 80 and 200 m. There is also a tendency for the optical activity to be found at the interfaces; this is, of course, due to the fact that some gradients in T and S must be present before any signal will be seen by the shadowgraph system. Since both T and S decrease with depth, most of the observed activity is consistent with salt fingering; however, due to the relatively weak contrasts found on this dive and a somewhat dirty optical system, none of the photographs provide very convincing evidence of finger activity.

One can also examine the coincidence of mixing activity with the shears measured by the SCIMP current meters. Figure 3b shows profiles of U, V and shear squared along with a profile of mixing type. The V axis shows less variability at small vertical scales than the U axis, a feature noted by Gargett *et al.* (1981). This is probably due to the asymmetries in the vehicles drag distribution and differences between the moments of inertia of the two axes. Since the response function of the vehicle is unknown, we have computed shear squared by summing the squared shears of the two components. Shears were computed by a least squares fit of $U(z)$, $V(z)$ over 15 adjacent points, about 3 m, for this figure.

We can make an estimate of the average low wavenumber contribution to shear

squared that is not detected by SCIMP, from the composite shear spectrum presented by Gargett *et al.* (1981). Integration of their spectrum from low wavenumbers to 0.1 cpm suggests that a shear squared level of about 2×10^{-5} S^{-2} would be unresolved by our instrument. As can be seen in Figure 3b, this level is often greater than the low level shears seen by SCIMP, but significantly less than the maximum values. Thus we expect to make reasonably good estimates of shear squared in the high shear events.

Unfortunately, there was a noise problem with the velocity data on this first dive (corrected on later dives) and some of the particularly sharp peaks are spurious. Relatively few of the patches of mixing activity appear to correlate with high shears; only the activity immediately above 50 db is obviously associated with a high shear event. A quantitative check on the correlation between mixing activity and Richardson numbers and density ratios will be made in Section 4.

Our second SCIMP dive was made in the front associated with the North Atlantic Current. Temperature, salinity, σ_θ, and mixing activity are profiled in Figure 4a. A dramatic difference can be seen in temperature and salinity profiles of this frontal station as compared to Dive 1. Prominent intrusions in T and S are seen with amplitudes as large as 2°C and 0.2‰ and with vertical scales from 10 to 50 m. There was also much more mixing activity as indicated by the shadowgraph films. The strongest events are found at the boundaries of the intrusions. As can be seen in Figure 4b, there was no dramatic increase in the velocity variance, in fact, the profiles appear to be less energetic because of the absence of noise spikes. Some of the mixing events can be correlated with high shears. Little correlation between the velocity profiles and the intrusions can be seen. This is expected because the estimated intrusion velocities are much less than the rms internal wave velocities. The overall incidence of mixing activity was an order of magnitude larger than on Dive 1, with 17% of the frames having received a contrast grade greater than zero.

We feel that the presence of the strong thermohaline intrusions is the main

---

Plate 1. The diagram in the upper right shows the configuration of the mirror and support struts which cause the dark shadows seen in the photographs. The photographs on the right are typical of most of the water column, very little mixing activity is usually seen. The vertically banded striations on the left are salt fingers acting on the underside of a strong warm-salty intrusion seen in the temperature and salinity profiles in the center of the diagram.

Plate 2. Examples of quiet, turbulent and fingering regions from Dive 2.
05598 and 07462 = quiet
05806, 05811, 05817, 05822 = isotropic turbulence
07162 = tilted salt fingers
07168, 07173 = salt fingers

Plate 3. Photographs from Dive 3, near the bottom of a warm-salty intrusion. Images 18390 through 18430 show both isotropic and fingering structures. Images 18815 and 18820 are from an inactive mixed layer below the high gradient region.

SALT FINGERS

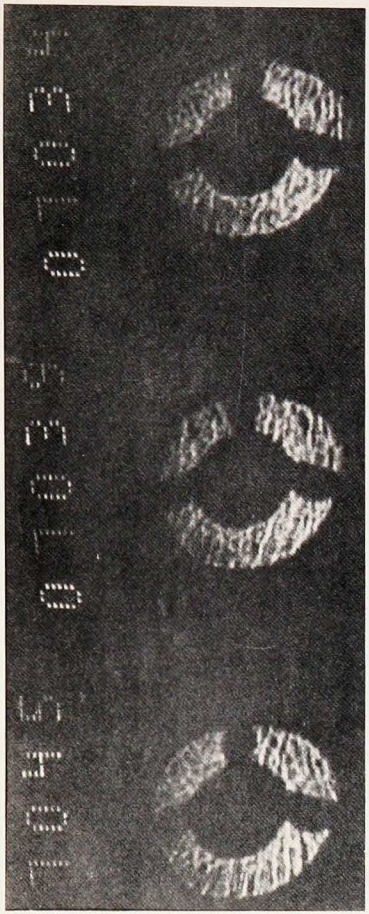

SCIMP 10-2, 4/17/80, 46°29'N, 41°46'W
Sink rate = 14.6 cm/s, Frame rate = 1.1 Hz

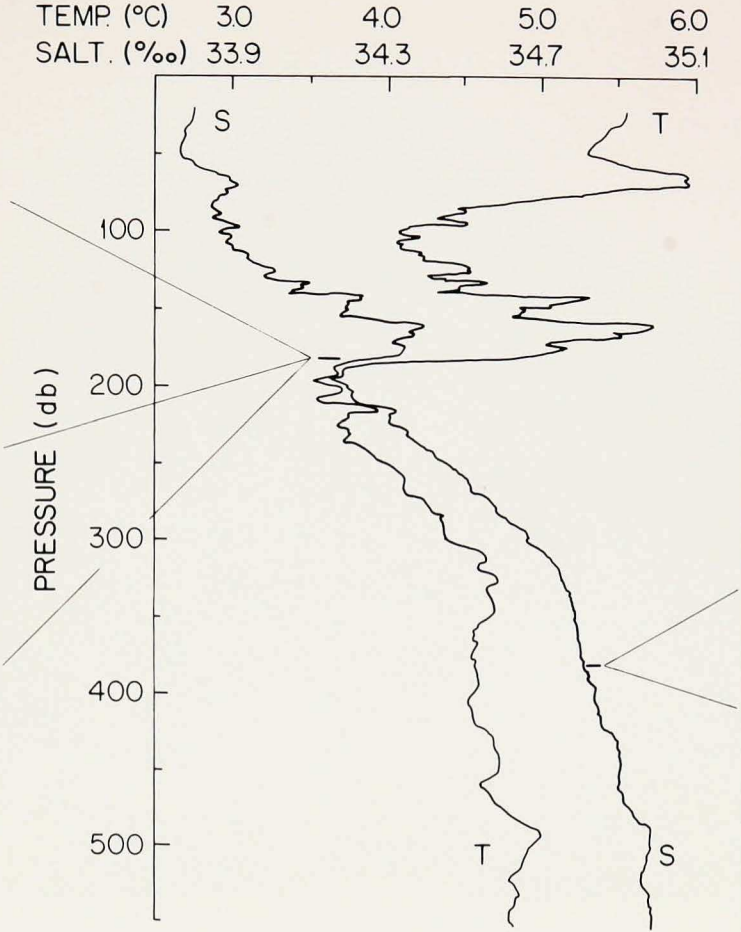

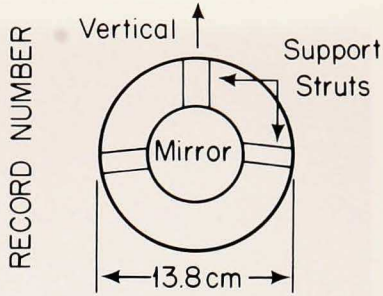

QUIET REGION

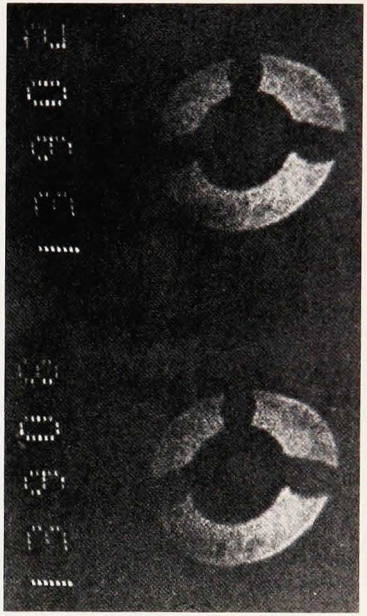

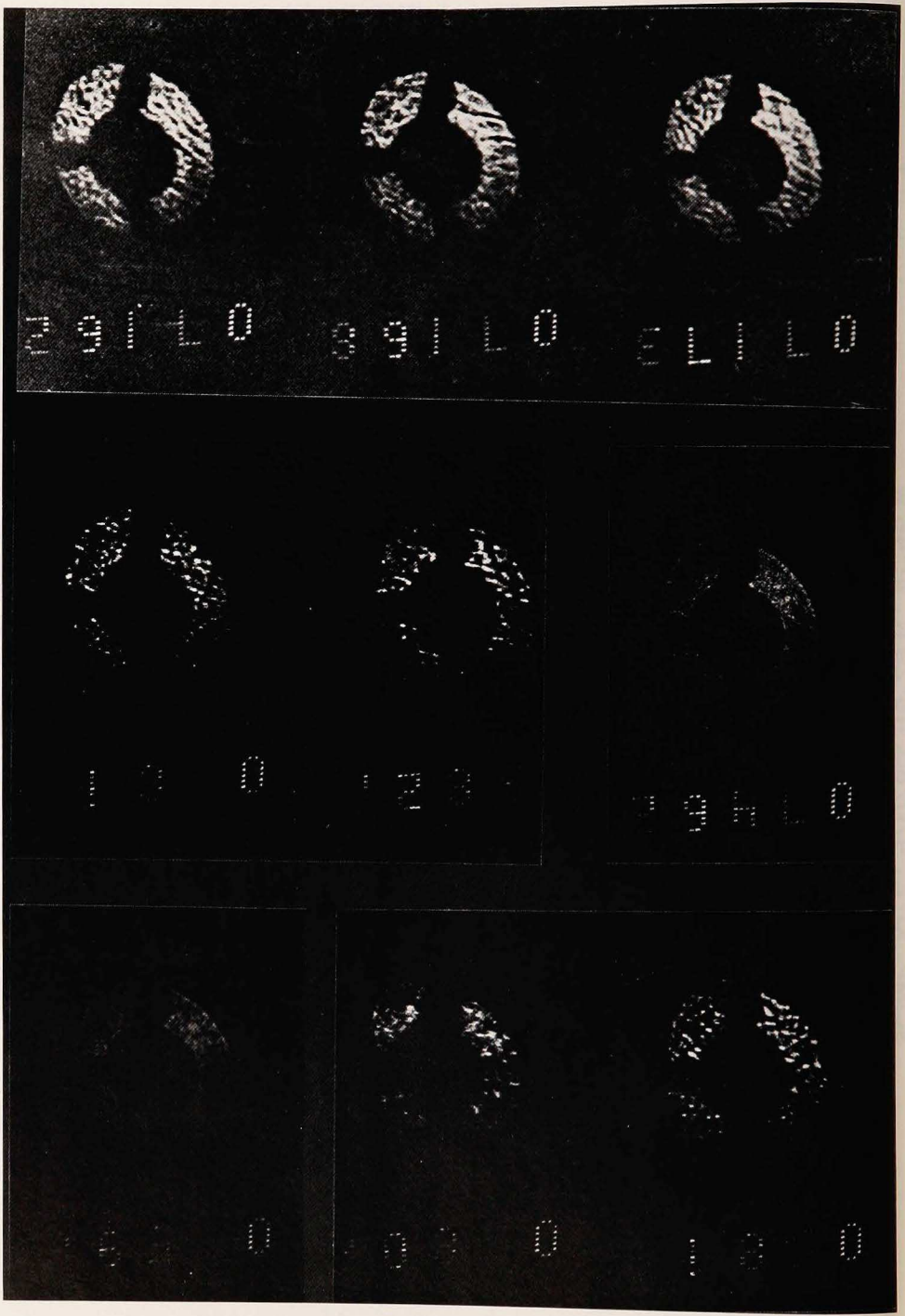

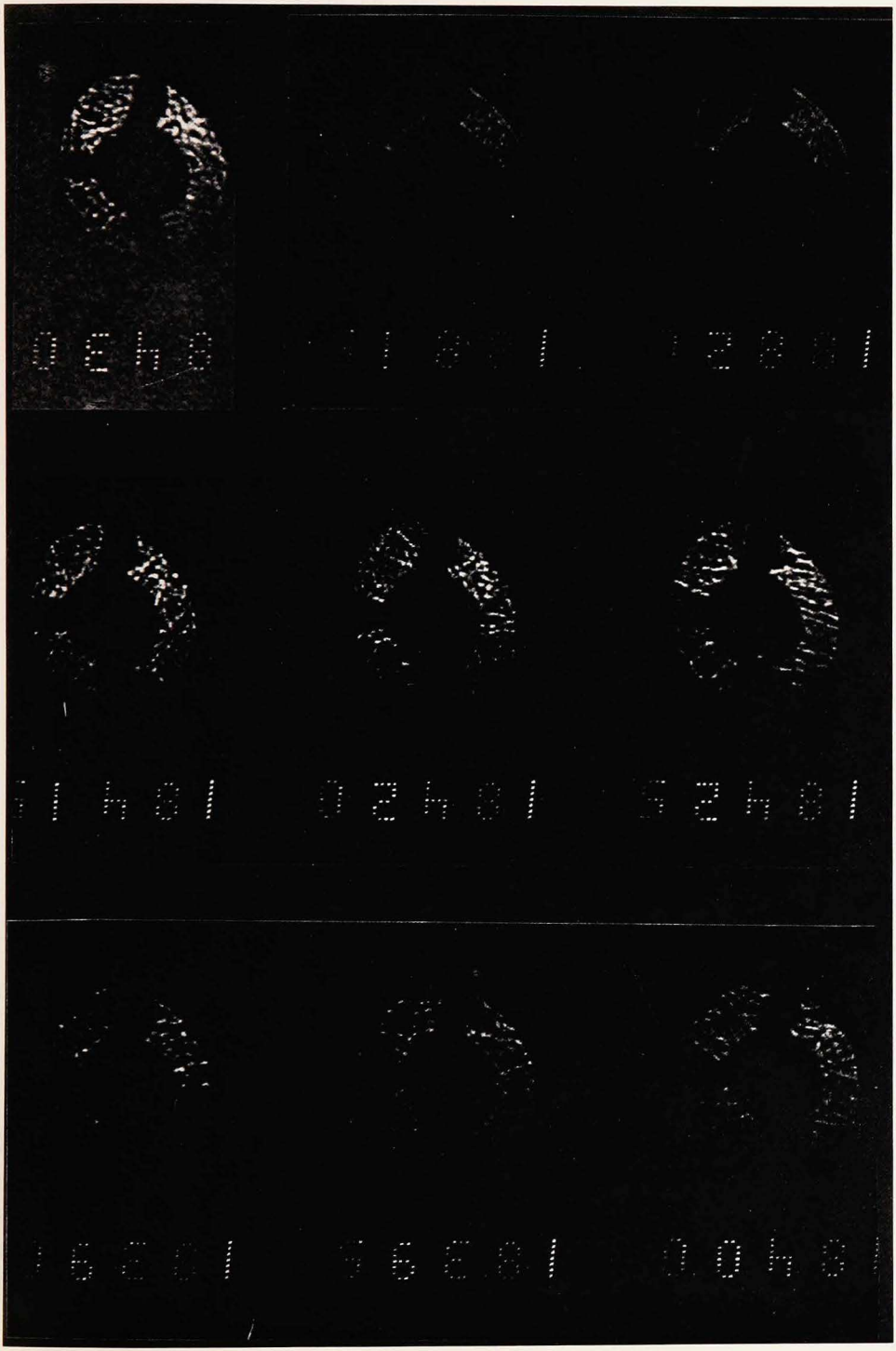

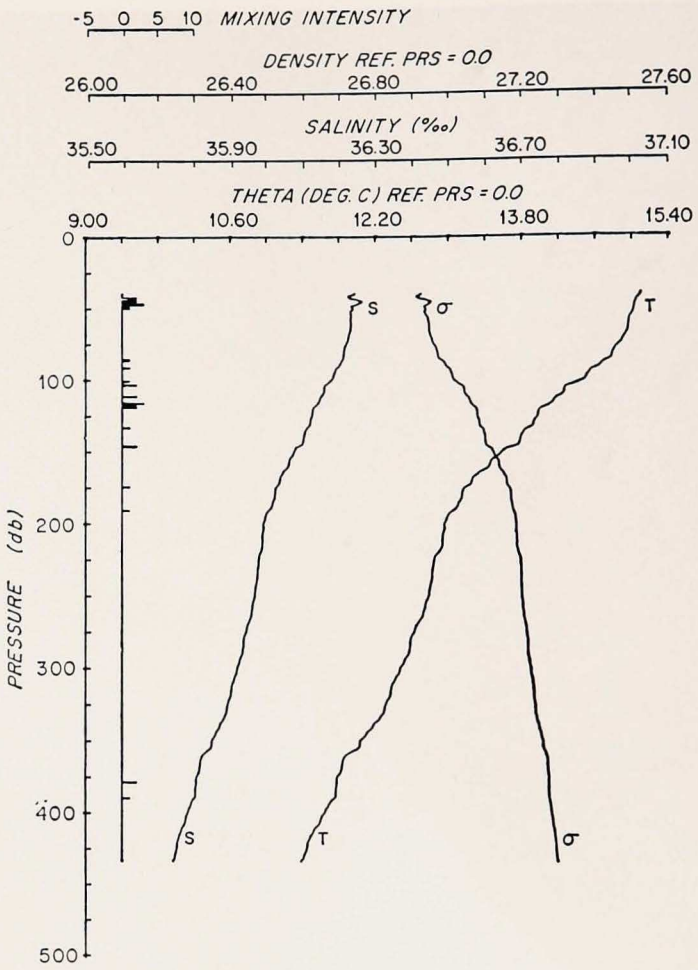

Figure 3a. Potential temperature, salinity, σ_θ and mixing intensity from SCIMP dive one.

cause of the increased mixing activity. Since double-diffusion is expected to act on the boundaries of such intrusions and no obvious increase in shear activity is apparent, it is likely that most of the mixing is double-diffusive. A quantitative assessment of this statement will be made in Section 4, however, examination of the data in more detail helps to identify instances of both shear instability and salt finger activity. We will review two mixing events more closely: a patch of isotropic turbulence at about 150 db and the salt fingers already shown in Plate 1.

In Figure 5a are expanded plots of T, S, $\sigma_{.15}$ (where σ_z is the potential density anomaly referenced to $z \times 10^3$ dbars) and mixing intensity plotted against record number to allow correlation of the profiles with the photographs on Plate 2. As can be seen in the data there are strong salinity-compensated temperature inver-

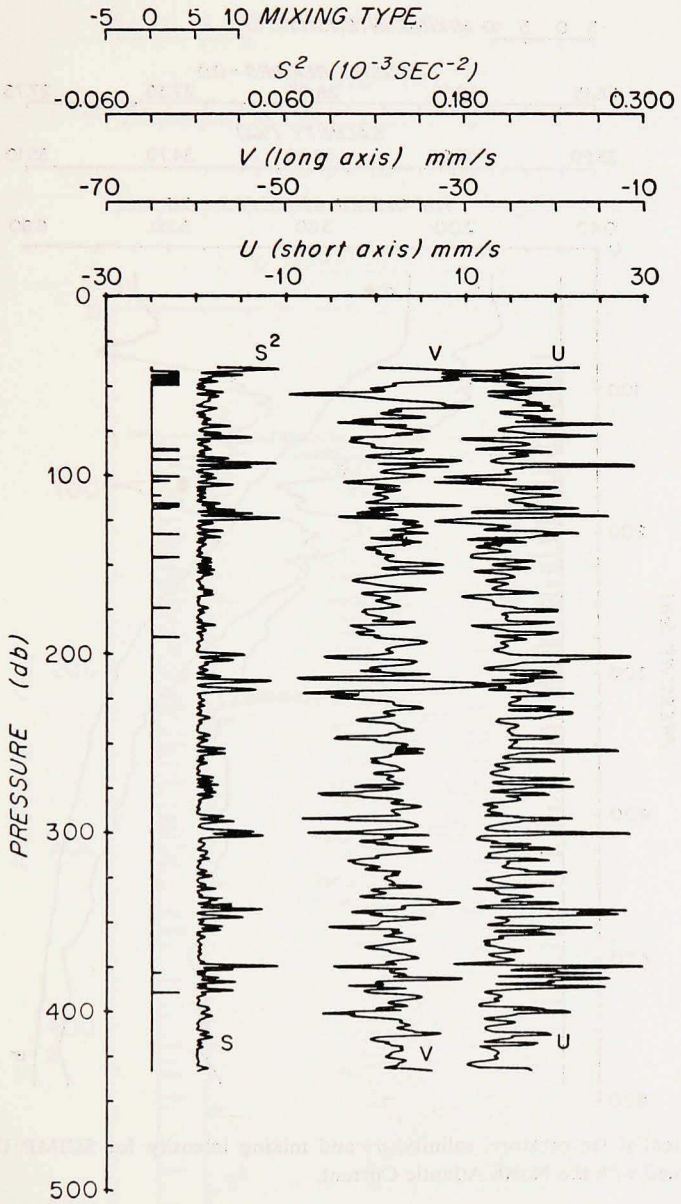

Figure 3b. Profiles of U (perpendicular to the optical axis of SCIMP), V (aligned with the optical axis), shear squared (computed over about 3 db) and mixing type for SCIMP Dive 1.

sions which do not show in the density profile. However, some small-scale inversions in density are apparent, over vertical intervals of about 1 m. These tend to be regions where strong isotropic activity is observed on the shadowgraph films. Thus,

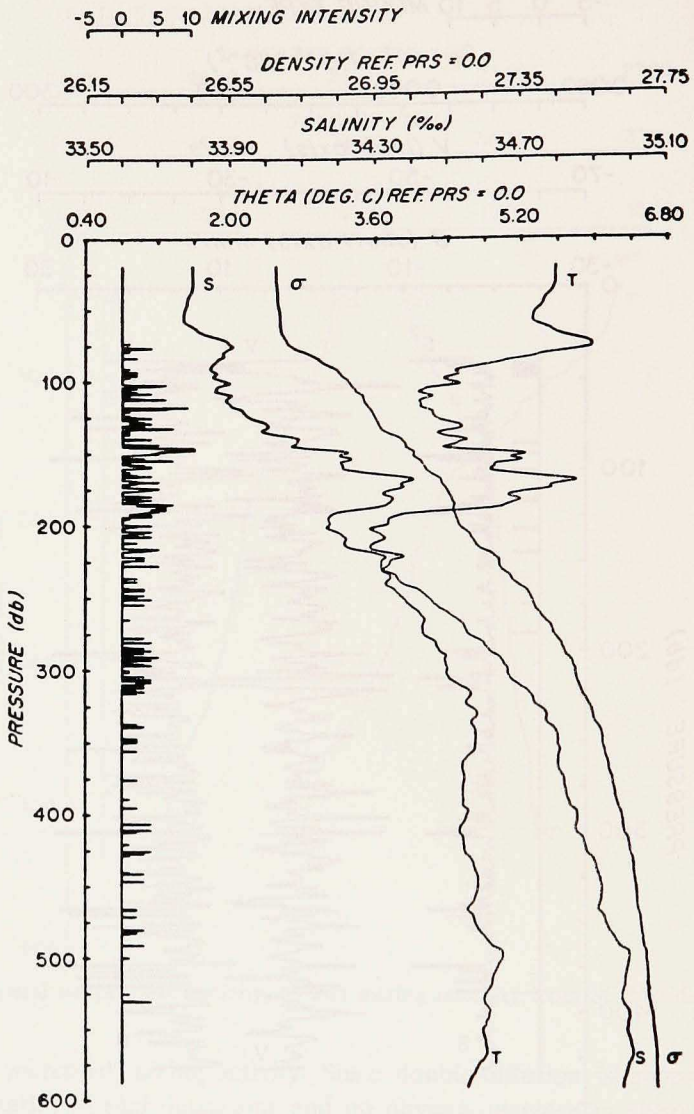

Figure 4a. Potential temperature, salinity, σ_θ and mixing intensity for SCIMP Dive 2, in the front associated with the North Atlantic Current.

we are inclined to believe that these inversions are real and not an artifact of the data processing (i.e., an error in the lag correction). The patch of activity near Record Number 5800 is a particularly good example of an isotropic mixing event as seen in the sequence of photographs in Plate 2. In Figure 5b, we have plotted the individual velocity profiles, mixing type and shear squared. The shears were

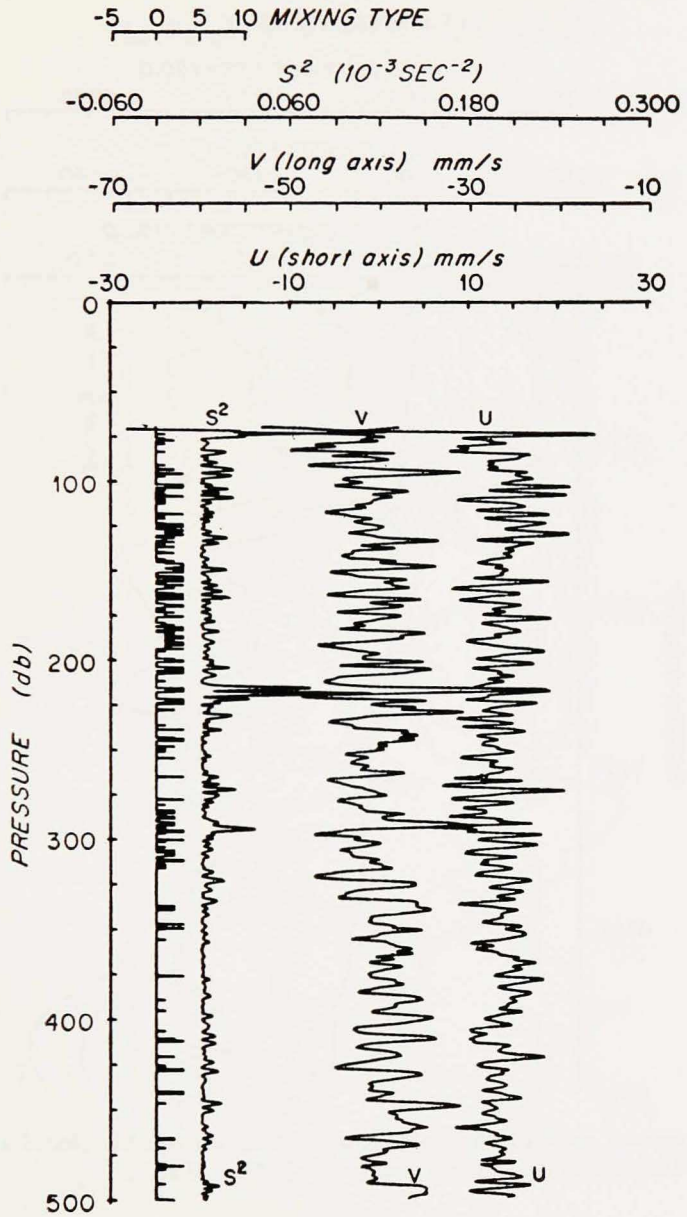

Figure 4b. *U*, *V*, shear squared and mixing type for Dive 2.

computed in this case by least squares fits over five adjacent points, covering about 0.9 m. Many of the mixing events are correlated with high shears. The density overturns above Record Number 5800 and near 6050, in particular, have moderate shear

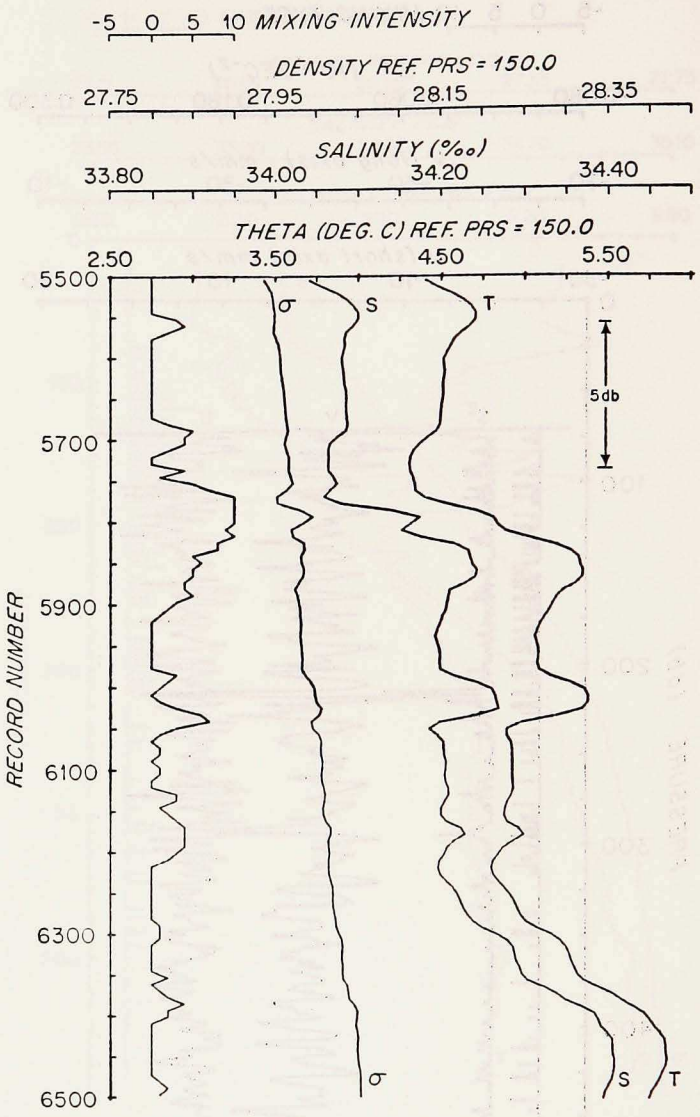

Figure 5a. Expanded profiles of $\theta_{.15}$, salinity, $\sigma_{.15}$ and mixing intensity plotted against Record Number to allow correlation with the photographs in Plates 1 and 2.

associated with them. Since the mixing type classification is clearly isotropic (3), we have interpreted these events as instances of shear instability.

The second event we will examine in detail is the patch of salt fingering just above 200 db. Figure 6a contains the temperature, salinity, $\sigma_{.2}$ and mixing intensity profiles as a function of record number; Figure 6b, has the velocities and

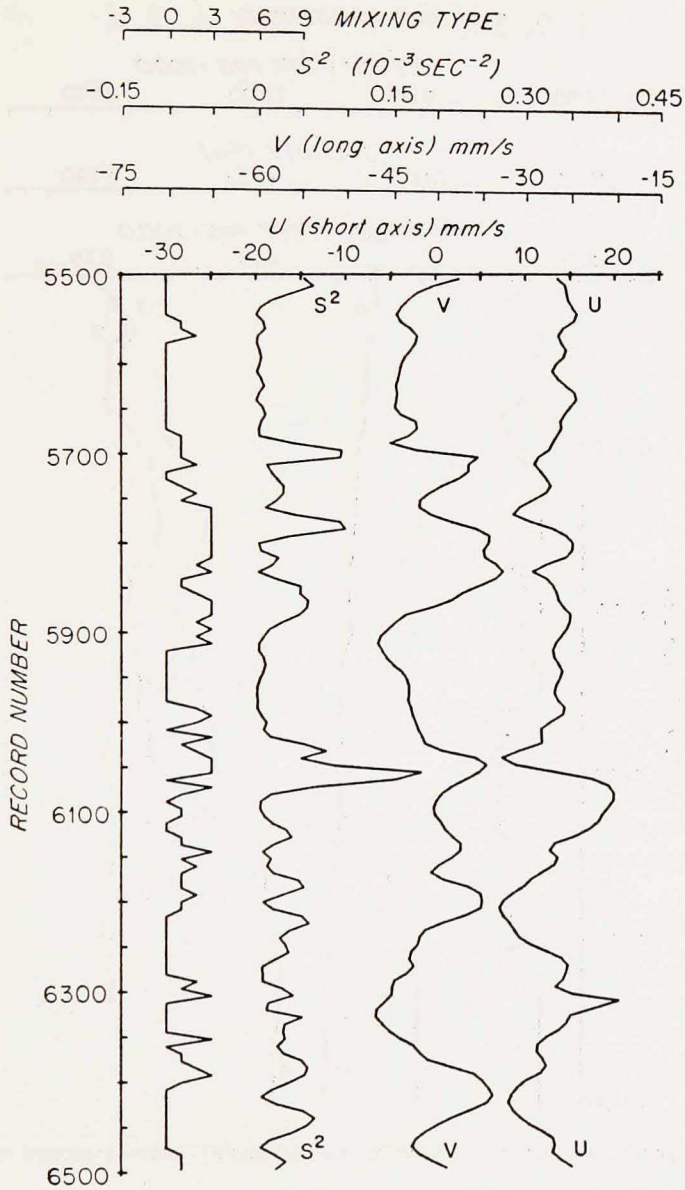

Figure 5b. *U*, *V*, shear squared and mixing type plotted against Record Number for Dive 2.

shear squared estimates. Corresponding photographs from this interval can be seen in Plates 1 and 2. The most prominent feature in this interval is the patch of vertically aligned striations associated with the warm-salty over cold-fresh interface between Record Numbers 7000 and 7200. Activity is seen above and below

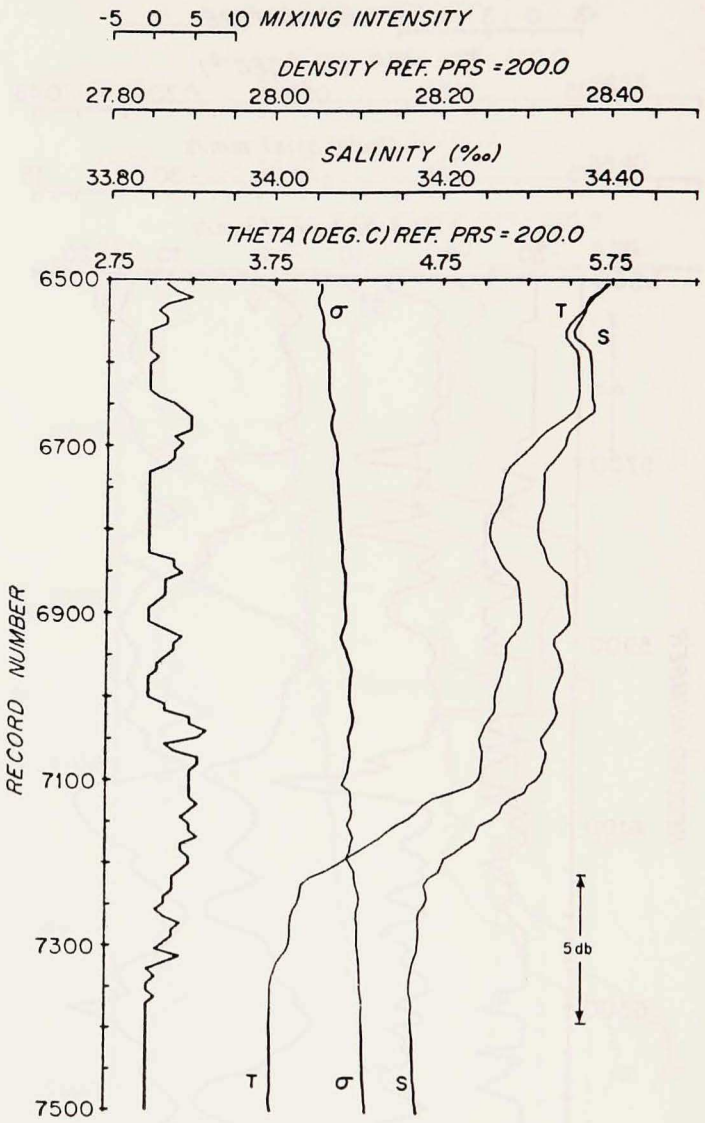

Figure 6a. Expanded profiles of $\theta_{.2}$, salinity, $\sigma_{.2}$ and mixing intensity plotted against Record Number.

this interface as well, in the regions of reduced gradients. These images are entirely consistent with salt finger activity on the bottom interface of this intrusion. These are, in fact, the clearest images of salt finger activity we have obtained. One reason for the clear striations is suggested by the velocity profiles which give at least an indication of the high wavenumber structure. We see that there is mod-

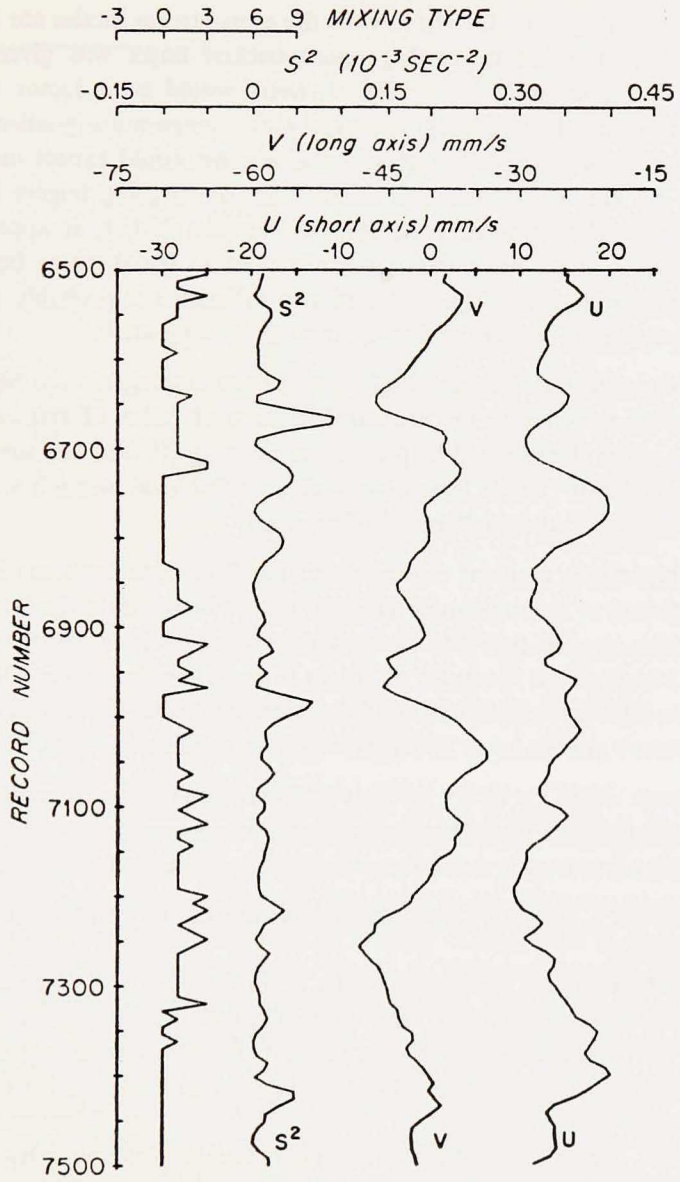

Figure 6b. *U*, *V*, shear squared and mixing type plotted against Record Number for Dive 2.

erate shear in the *V* component, aligned with the optical axis, and very little shear in the cross axis component in this interval. Thus, these vertical bands are most likely indicative of salt 'sheets' aligned with the flow rather than salt fingers. Linden (1974) showed that fingers form sheets aligned with the current because the down-

stream modes are damped by the shear while the cross-stream modes are unaffected. The half width of the fastest growing square-packed finger was given by Stern (1960) as $L = \sqrt{2}\ \pi\ (g\alpha\bar{T}_z/\nu K_T)^{1/4}$. Salt sheets would be a factor of $(\sqrt{2})^{-1}$ narrower than fingers. Thus, for the observed mean temperature gradient of about 0.01°C/cm and appropriate values of α, ν and K_T, we would expect sheets with a half-width of 1.1 cm, a complete pair of up- and down-going fingers in 2.2 cm. From viewing the photographs, (i.e., Record Number 7045), it appears that a spacing of about 1 cm is most frequently observed as the distance between two maxima in image brightness. The factor of two difference is probably not significant, but three explanations for the discrepancy can be suggested:

(1) we must recall that the shadowgraph technique emphasizes the higher wavenumbers, being sensitive to the second derivative of index of refraction. Thus, if there is a range of sheet widths present, as Schmitt (1979a) has suggested and Gargett and Schmitt (1982) have observed, then the shadowgraph will have an enhanced response to the smaller-sized sheets.

(2) The temperature gradient estimated for the 2 m-thick interface is probably an underestimate of the maximum temperature gradient within the interval. That is, the filtering applied prevents us from determining whether there is actually a series of interfaces on the order of 10 cm thick or one large one. Observations by Williams (1975) suggest that multiple interfaces occur frequently. Thus, the true temperature gradient may be larger, resulting in thinner fingers.

(3) The sheets might be closer to an equilibrium state than a rapidly growing state. Schmitt (1979a) finds that equilibrium fingers can be ¼ as wide as the fastest growing fingers at low density ratios.

Thus, the observed 1 cm-wide sheets are well within the range of widths predicted for growing fingers.

Encouraged by the good agreement of the observed vertical bands with the predicted wavenumber of growing salt sheets, there is little doubt that these structures were caused by double-diffusive convection at the bottom boundary of a warm, salty intrusion. No other known instability could produce features with such a tall and narrow aspect ratio.

We now turn our attention to our efforts to combine SCIMP dives with the lateral mapping of intrusive finestructure with CTD Tow-yo's.

3. Correlations between lateral intrusions and double-diffusive mixing

Two attempts to perform simultaneous SCIMP dives and CTD Tow-yo's between the surface and 500 db were made. The navigation during these Tow-yo's is shown in Figure 7, along with the positions of SCIMP deployments and recoveries. In the first Tow-yo, we obtained a more successful correlation between the SCIMP

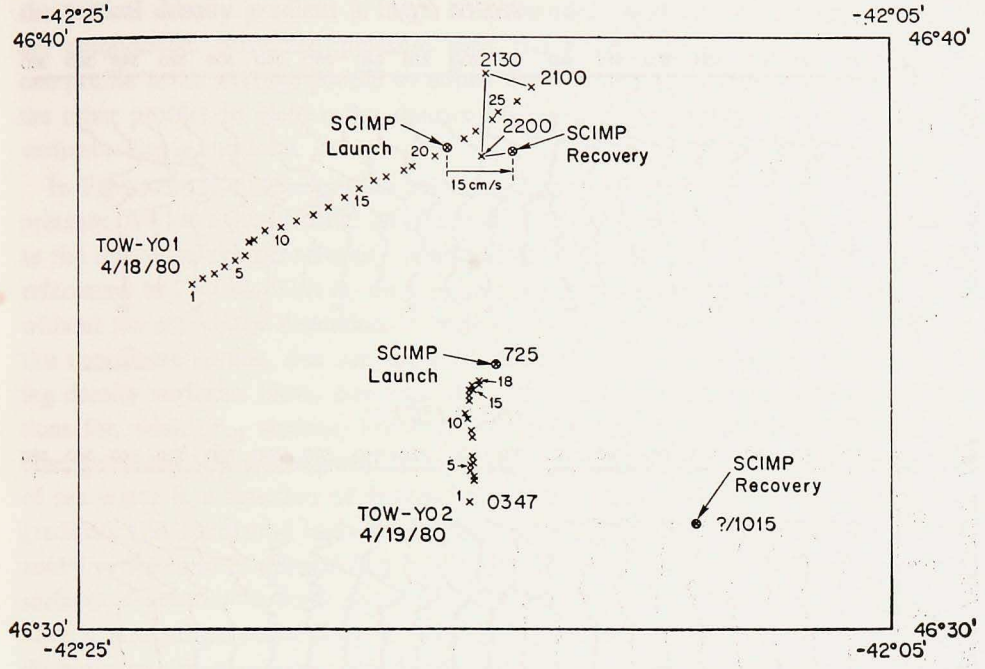

Figure 7. CTD cast locations for Tow-yos 1 and 2, with SCIMP launch and recovery positions. Odd numbered casts are down, even numbered are up.

and CTD profiles; the comparison in the second Tow-yo was not as good because of a delayed SCIMP launching. Our original conception of a north-south orientation to the front, suggested by the historical mean isotherm positions, was disturbed by the eastward displacement of SCIMP during Dive 3. Unfortunately, our ship time was limited, and we were unable to survey the mesoscale structure of the front. Satellite infrared photos made of this region during our experiment reveal that a large meander existed in the North Atlantic Current, so that the front was oriented in an easterly direction (T. Green, personal communication). This is consistent with the SCIMP displacement, which suggests an eastward current of 15 cm/s averaged over the upper 900 db. Thus our first Tow-yo was largely along-front rather than across-front; a conclusion which may affect our later interpretation of the role of these intrusions in cross-frontal mixing.

Successive temperature profiles from this Tow-yo are shown in Figure 8a. Each profile has been offset 1.5°C. An approximate horizontal length scale is shown; the profiles are about 500 m apart. A closer spacing would have been desirable. However, it was difficult to maneuver the ship at lower speeds and also difficult to lower the CTD at a higher rate, since the instrument was deployed from the stern U-frame to free the starboard side for the SCIMP operations. Even with the 500 m

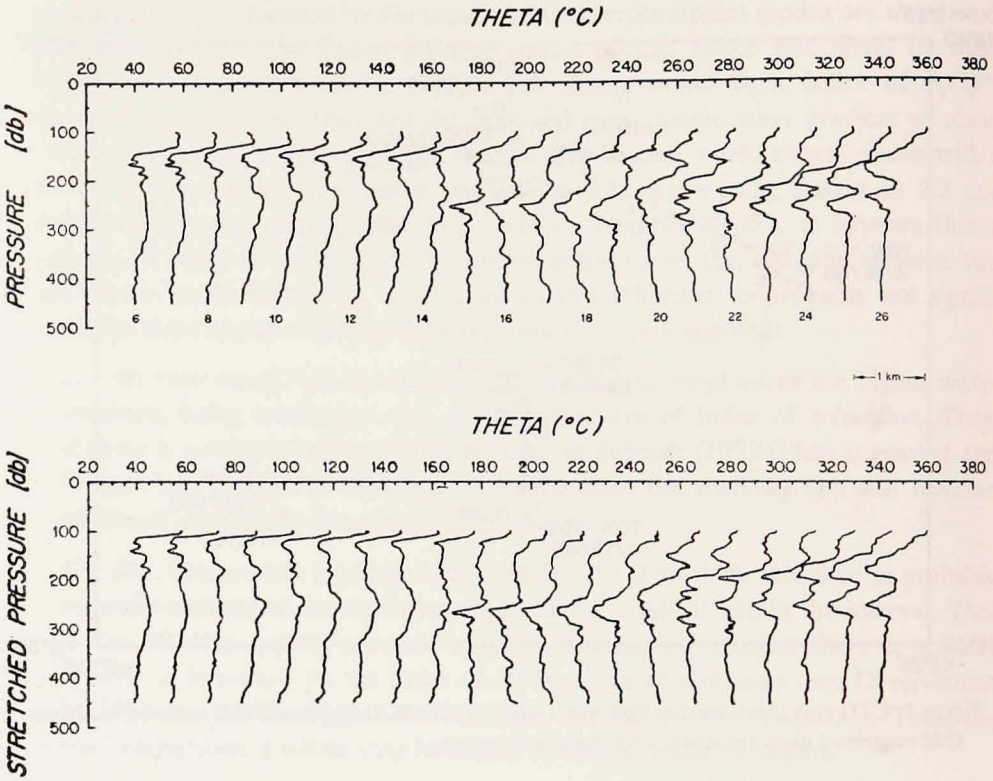

Figure 8. (a) Series of temperature profiles from Casts 6 through 26 from Tow-yo 1. Each profile has been offset 1.5°C. (b) Temperature profiles plotted against stretched pressure. The potential density-pressure relationship from Cast 20 (immediately before the SCIMP launch) was used to stretch the other profiles.

separation between profiles, one can see correlation of 10 to 50 m-thick intrusions across several profiles. In the more easterly profiles, some features appear to be coherent for as much as 5 km horizontally.

In order to determine whether the observed intrusions cross density surfaces as predicted by Stern (1967), it is necessary to remove the vertical displacements of the intrusions due to internal waves. On horizontal scales of 1 km, one expects the vertical displacements due to internal waves and the effects of double-diffusion to be comparable. Joyce *et al.* (1978) resorted to using a stretched pressure vertical coordinate (Johnson *et al.*, 1978) while Gregg (1980) used potential density as the independent vertical coordinate. The latter presentation works well when the Brunt-Väisälä frequency is relatively constant throughout the vertical interval of interest. However, when the vertical stability changes significantly, then plotting against potential density introduces an undesired vertical distortion; regions where

the vertical density gradient is large are expanded, while regions of low gradient are compressed. Stretched pressure uses the pressure-density relationship from one profile or an average profile to adjust the pressure-temperature relationship of the other profiles to yield a flat density field and an approximate preservation of vertical scales is obtained.

In Figure 8b, the same profiles shown in Figure 8a are plotted against stretched pressure. We have used Profile 20 (the upcast profile prior to the launch of SCIMP) as the reference pressure-density relationship. We have used the potential density referenced to 250 db. This is, thus, equivalent to plotting profiles against $\sigma_{.25}$, but without the associated distortion of vertical scales that such a plot would yield. In this coordinate system, one can see evidence that some of the intrusions are crossing density surfaces. Note, however, that one must be careful of such interpretations for, while $\sigma_{.25}$ surfaces are everywhere flat, potential density referenced to other pressures will not necessarily be level. This arises because the compressibility of sea water is a function of temperature and salinity, and both have significant gradients (on horizontal and/or isopycnal surfaces) in frontal regions. The horizontal variation in compressibility can lead to 10 to 20 m displacements of isopycnal surfaces referenced to some other pressures. To better illustrate this problem, we have contoured potential density (Figure 9a) referenced to the surface and 500 db in the stretched pressure coordinate system (reference pressure 250 db). Large vertical displacements of the isopycnals (σ_θ and $\sigma_{.5}$) occur near the horizontal terminations of major intrusions (e.g., below 300 db between Casts 4 and 5). An alternative to using a stretched pressure coordinate system with a single reference level is to use a series of reference levels as in the leveling technique of Bray and Fofonoff (1981).

In Figure 9b, we present a computer contoured potential temperature section with stretched pressure. A contour plot of potential temperature obtained with the procedure of Bray and Fofonoff, though not directly comparable, was similar and is not shown. In viewing Figure 9b, we focus primarily on features near 250 dbars. One can see evidence of an intrusion crossing density surfaces in the right half of the diagram, between Casts 17 and 23, above 200 stretched decibars. Other intrusions show little or no slope. The slope of this feature, 0(1 m/100 m) is similar to that reported for intrusions in other fronts (Toole and Georgi, 1981, Table 1).

SCIMP Dive 3 was made between upcast 20 and downcast 21, and sampled the strong intrusion above 200 db. A comparison of the temperature profiles from the SCIMP dive and the two CTD casts is given in Figure 10. In this figure the two CTD casts were stretched relative to the SCIMP profile. As can be seen in the figure, the three temperature profiles are remarkably well correlated with one another, especially in the upper 300 m. Based on the ship's speed, we judge that these three casts were made within a few hundred meters of each other. The

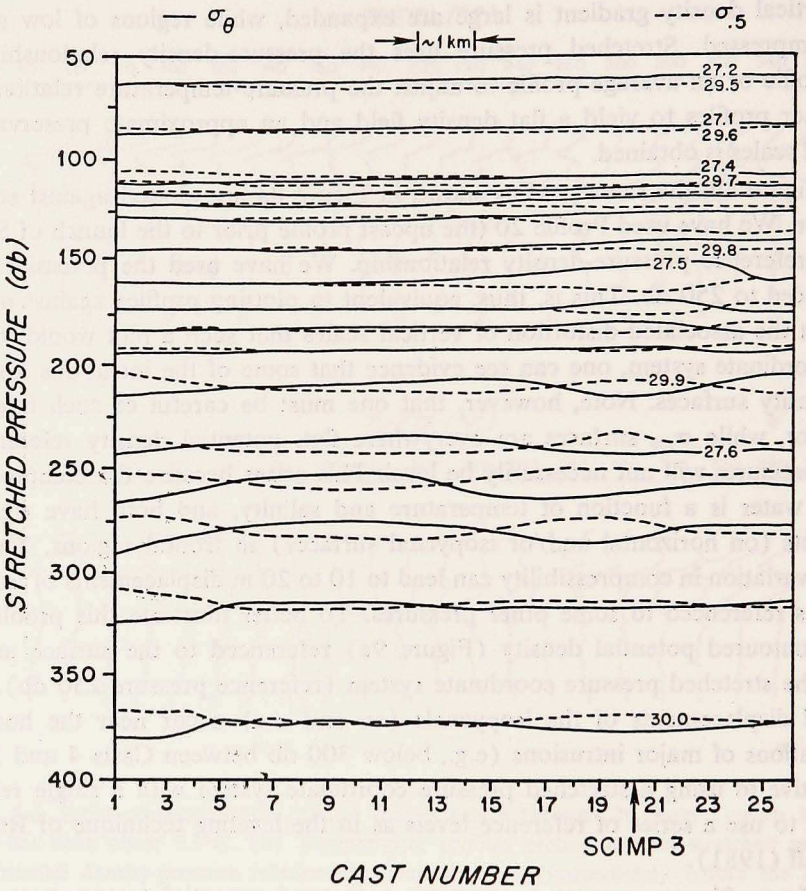

Figure 9a. Computer-drawn contours of σ_θ surfaces (—) and $\sigma_{.5}$ surfaces (— — —) against stretched pressure referenced to 250 db. The $\sigma_{.25}$ surfaces are flat, but σ_θ and $\sigma_{.5}$ surfaces show significant displacements, especially where there are strong lateral temperature gradients.

strong interface at 200 stretched db, the bottom of the warm-salty intrusion, was particularly active with optical microstructure as can be seen in profiles of T, S, σ_θ and mixing intensity in Figure 11. Plate 3 contains photographs from the region of the interface, several of which have strong vertical bands, implying active salt fingering at the bottom of the intrusion. An expanded view of this region is given in Figure 12 where profiles have been plotted against Record Number. The expanded profiles show that the bottom of the intrusion is not just one interface but several (4 or 5), each 15-50 cm thick, separated by 2 m-thick mixed layers. Examination of the photographs reveals that vertical bands are more likely to be observed at the interfaces; isotropic structures are likely to be found in the weaker gradient layers. This multi-layered structure is consistent with the ocean observations of Williams (1975), and the salt finger experiments of Linden (1978).

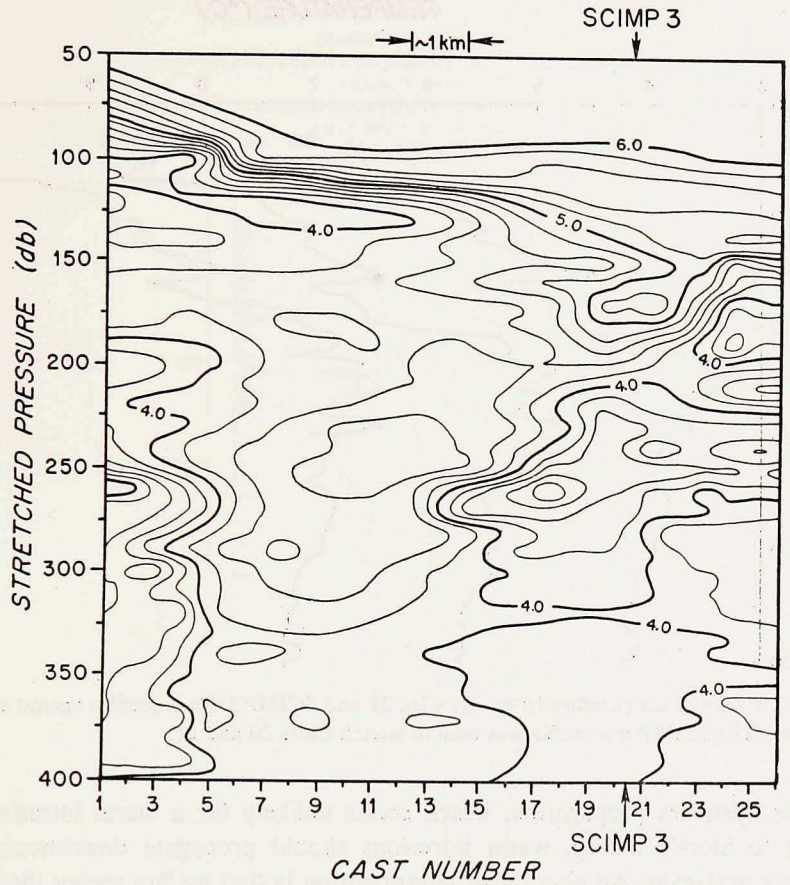

Figure 9b. Computer-drawn contours of potential temperature against stretched pressure for Tow-yo 1.

We feel that these photographs demonstrate rather convincingly that active salt fingering was occurring in association with an intrusion having a significant cross-isopycnal slope. Thus the physical mechanism of the double-diffusive generation of intrusions, as proposed by Stern (1967), must be considered a viable explanation for the behavior of the observed intrusive finestructure.

One of the predictions of Stern's theory is that warm-salty intrusions should rise, while cold-fresh intrusions should sink across density surfaces due to the excess flux of salt by the fingers. One is tempted by the contour plots of Figure 9 to say that the origin of the warm-salty intrusion is to the right, and that it is propagating downward across density surfaces to the left. However, this is more an accident of the contouring and the inadequacy of our knowledge about the detailed structure of the front. Propagation of the warm, salty intrusion to the left also

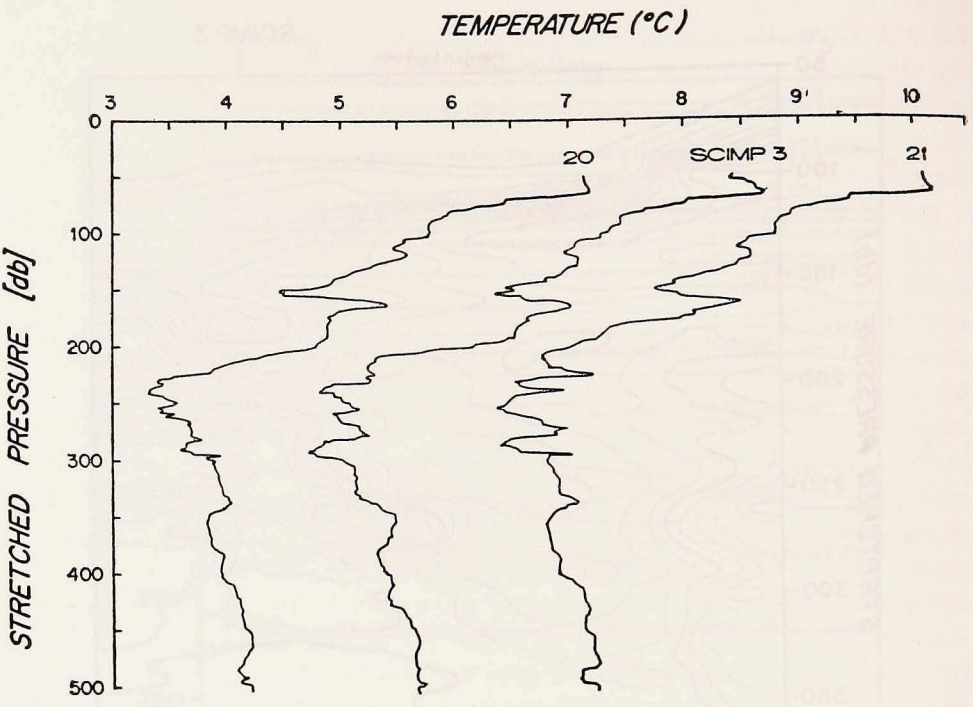

Figure 10. Potential temperature from Casts 20, 21 and SCIMP Dive 3 profiles against stretched pressure. The SCIMP $\sigma_{.25}$ profile was used to stretch Casts 20 and 21.

indicates upstream propagation, which seems unlikely for a warm intrusion. According to Stern's theory, warm intrusions should propagate downstream, cold intrusions upstream. An alternative interpretation is that we are seeing the merger of this feature with water of similar *T-S* properties. This is the predicted final fate of double-diffusive intrusions; they are expected to cross density surfaces until reaching a surface with the same *T-S* properties. Clearly, without more detailed mapping of the three-dimensional structure of the front and careful tracking of the intruding water mass, we can only claim consistency of the observed intrusions with the double-diffusive generation theory. However, there is no doubt that salt fingers are actively mixing the intrusions, if not causing them.

Our second Tow-yo and fourth SCIMP dive were not as successfully coordinated as our first attempt. The course of the Tow-yo is plotted in Figure 7. There is some uncertainty about the true location of the SCIMP recovery, as Loran reception was poor and no satellite fixes were available during the SCIMP recovery. Unfortunately, on this Tow-yo a very rough deployment of SCIMP caused the loss of one of its weights so that it did not sink. The Tow-yo had to be abandoned to retrieve SCIMP. We were able to redeploy SCIMP in a short time, doing so in the hope that we might still catch some of the features apparent in the CTD

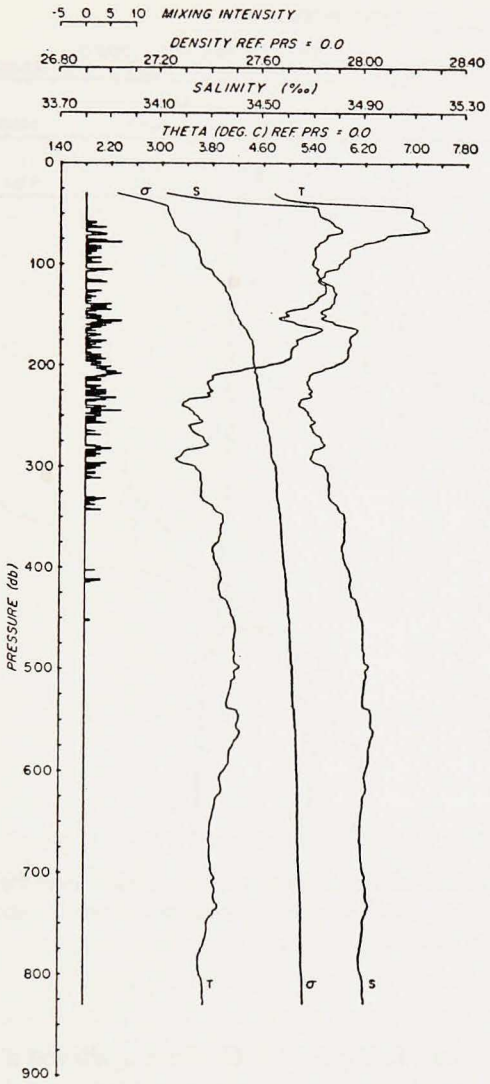

Figure 11. Profile of θ, salinity, σ_θ and mixing intensity for Dive 3.

profiles. However, a comparison of the SCIMP temperature profile and those of the last two Tow-yo casts, showed that we were not successful.

An additional problem with this dive was found in the optical system, which became misaligned due to the nontrivial impact between SCIMP and the ship's hull during deployment. The resulting shadowgraphs show a distorted image of much lower quality than the photos from Dives 2 and 3. However, it was still possible to grade the films on mixing type and intensity. Profiles of T, S, σ_θ and

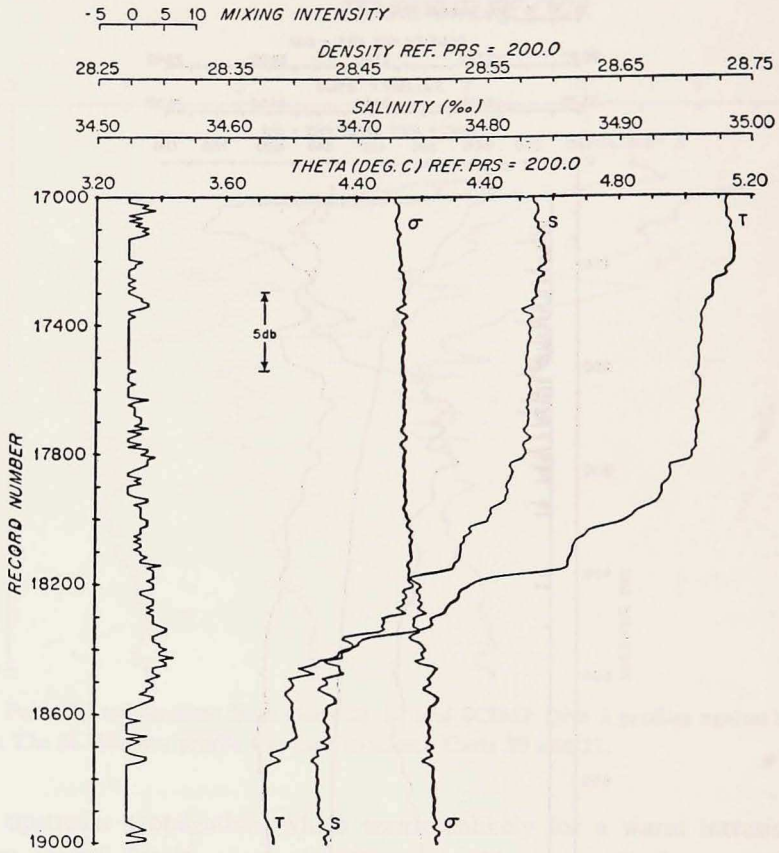

Figure 12. Expanded profiles of $\theta_{.2}$, salinity, $\sigma_{.2}$ and mixing intensity at the bottom of the warm-salty intrusion. The profiles are plotted against Record Number to allow comparison with the photographs in Plate 3.

mixing intensity are shown in Figure 14. One can again see a tendency for optical microstructure activity to occur on the boundaries of intrusions.

Despite the lack of coordination between the SCIMP Dive and the Tow-yo, the Tow-yo itself was perhaps more successful than our first effort. In Figure 13, the potential temperature profiles for the first nine casts are plotted against stretched pressure (referenced to 100 dbars). Again there are some features that show significant cross-isopycnal tilts, especially the thin intrusions near 100 db at the beginning of the tow. The 25 dbar thick warm intrusion centered near 110 db on the first lowering is some 20 db shallower on the sixth lowering. Since this Tow-yo was oriented in a more northerly direction, it should represent more of a cross-front than along-front section.

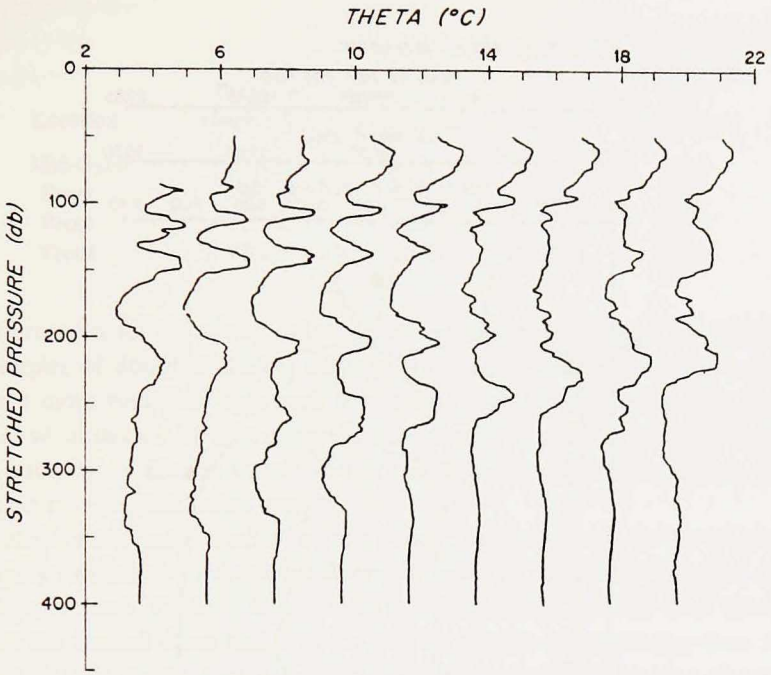

Figure 13. Potential temperature plotted against stretched pressure for the first nine casts of Tow-yo 2.

When Toole and Georgi (1981) considered the problem of the generation of double-diffusive intrusions, they extended the original analysis of Stern (1967) to include the effects of friction. With the stability analysis, they investigated the relationship between the vertical scale and cross-isopycnal tilts and various other environmental parameters. Based on their analyses, we expect greater slopes across density surfaces for across-front than along-front tracking of intrusions. They also predict that small intrusions will show greater slopes than thick intrusions. Since the features seen in Figure 13 are, in general, thinner than the intrusions of the first Tow-yo; these data are consistent with both explanations. Also, we are more certain that the origin of the warm intrusions is to the south, while the origin of the cold intrusions is to the north. Thus it appears that this Tow-yo provides convincing evidence that warm-salty intrusions are rising and cold-fresh intrusions are sinking across density surfaces, in the manner predicted by the double-diffusive models.

4. Statistical occurrence of mixing events

In the previous two sections, we have examined the relationship of optical mi-

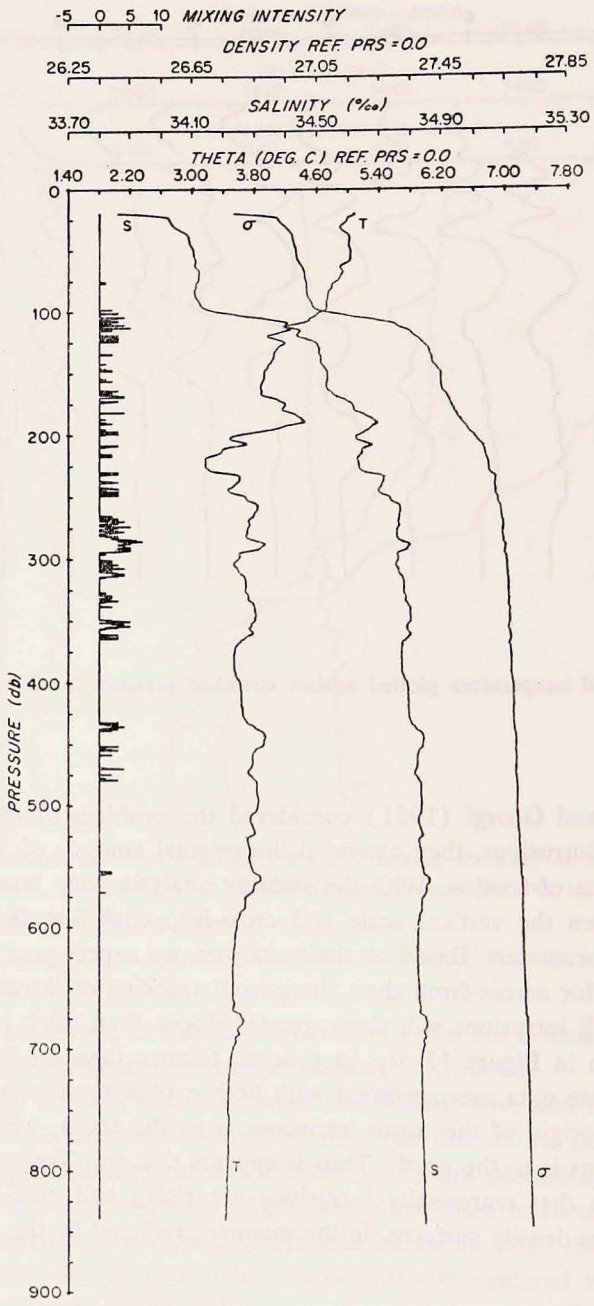

Figure 14. Profiles of potential temperature, salinity, σ_θ and mixing intensity for Dive 4.

Table 1.

Dive	Location	Pressure range (db)	Incidence of mixing events	Fraction of mixing events classified as: (1) vertical	(2) horizontal	(3) isotropic
1	Mid-Gyre	56-428	<0.02	0.14	0.24	0.62
2	Front	70-600	0.17	0.53	0.24	0.23
3	Front	55-465	0.27	0.47	0.27	0.26
4	Front	72-664	0.14	0.54	0.14	0.32

crostructure with temperature, salinity and velocity finestructure by showing specific examples of double-diffusive mixing and shear instability. In this section, we will take a more statistical approach to the data. While the optical data are largely a qualitative indicator of microstructure, and we are unable to objectively quantify the intensity of mixing events, we are able to examine the question of where mixing occurs in a quantitative way.

First of all, we can summarize the total occurrence of events in the various dives, with respect to both the overall incidence of mixing from each dive and the types of mixing observed. Table 1 is a summary of such data for the four dives. It reveals that the frontal dives had an order of magnitude more mixing than the mid-gyre dive. It also shows that a vertical orientation was most often observed, accounting for 51% of the events in the frontal dives while horizontal and isotropic structures accounted for 22% and 27%, respectively, of the activity. This is consistent with a double-diffusive classification of most of the activity at the front which we expect because of the strong interleaving. It also suggests that a vertical profiler may miss a significant fraction of the variance in microscale temperature gradients where vertical convective plumes due to double-diffusion are present. The factor of one to three usually applied to measurements of vertical temperature gradient variance to estimate the total variance, may be a substantial underestimate. Since salt fingers have aspect ratios of 10 to 30, an estimate of temperature gradient variance based on the vertical gradient alone may be 2 or 3 orders of magnitude low. Some method of measuring the intensity of small-scale lateral gradients is clearly necessary to quantify the mixing at oceanic fronts.

In order to identify the particular variables that most influenced the occurrence of optical microstructure, we have examined the probability of observing microstructure as a function of finestructure variables measured or computed by SCIMP. For example, we certainly expect that optical activity will be correlated with property gradients; no activity would be visible on the smallest scales if there were not gradients of T and S on meter scales. Since the index of refraction varies more like density than T or S alone, we have examined the incidence of optical activity as a function of N^2 ($= -g/\rho\ \partial\rho/\partial z$). Figure 15 shows the probability of observing microstructure for different ranges of N^2 for Dive 2. The trends shown in the figure

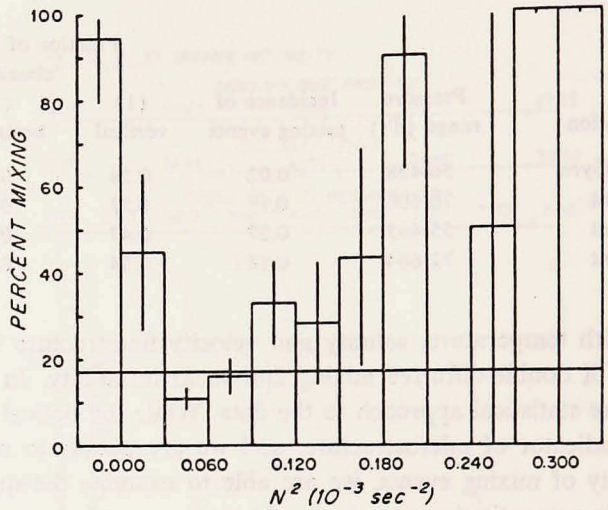

Figure 15. Percentage of observations of various values of N^2 which were associated with a mixing event for Dive 2. The horizontal line represents the null hypothesis (no correlation with N^2). The error bars are the 95% confidence intervals.

may be compared with the null hypothesis, that microstructure is independent of N^2, given by the horizontal line. The 95% confidence interval is shown based on the Clopper-Pearson estimator (Hollander and Wolfe, 1973) with a reduced number of degrees of freedom. It seems prudent to reduce the degrees of freedom based on two criteria. One is the run test applied to the optical data. It was found that the number of runs (mixing vs. non-mixing) was less than would be expected if all the data in the profile were independent of one another. A reduction in the number of degrees of freedom by a factor of $(2.6)^{-1}$ would be consistent with the number of runs observed and the given proportion of mixing versus non-mixing observations. This suggests that a typical vertical scale for a mixing event would be about 2.6×23 cm $= 60$ cm.

The second criteria was the auto-correlation length of the N^2 calculation. This depends, of course, on the vertical length scale used in the computation. For Dive 2, if N^2 is calculated by a least squares fit over five adjacent points, then the auto-correlation falls to 0.5 in less than two lags. If seven adjacent points are used, then the half-correlation point occurs at four lags. In order to match the space scales of the two variables, we have used five adjacent points to compute N^2 and reduced the number of degrees of freedom by the $(2.6)^{-1}$ factor suggested by the run test on the optical data. This yields a generous estimate of the error bars since one normally expects the cross-correlation length of two variables to be shorter than either of the two auto-correlations.

Figure 15 reveals that our earlier observation that unstably stratified regions

are often associated with mixing events is confirmed statistically, with 94% of the unstable regions having some optical activity associated with them. It also shows that regions with zero or very weak stratification also tend to be active as are the strongly stratified interfaces. Only the most frequently observed stratifications with $0.03 \times 10^{-3}\ S^{-2} \leqslant N^2 < 0.06 \times 10^{-3}\ S^{-2}$, were significantly less likely to have a mixing event associated with them. Thus, this analysis supports our initial impressions that mixing events tend to occur in association with both static instabilities and strongly stratified interfaces, and shows that events are less likely to occur under the most frequently observed stratifications.

Using this approach we have examined the data for evidence that mixing events are associated with the density ratio, $R\rho$, which governs the intensity of double-diffusive convection, and the Richardson number, Ri, which determines the possibility of shear instability.

The density ratio, $R\rho = \alpha T_z/\beta S_z$, where $\alpha = (-1/\rho)\ \partial\rho/\partial T$ and $\beta = (1/\rho)\ \partial\rho/\partial S$, must be greater than 1 and less than the ratio of thermal conductivity to salt diffusivity (about 100) for salt fingers to occur. For the diffusive case where cold-fresh water overlies warm-salty water, $0 < R\rho < 1$; and no double-diffusion is possible for $R\rho < 0$. Schmitt (1981) has suggested that salt fingers may be weak in general for $R\rho \geqslant 2$, only becoming a strong mixing process for $R\rho < 1.6$. This proposal is based on the rapid increase in finger growth rates as $R\rho \to 1$ and the observed occurrence of thermohaline staircase-type finestructure for $R\rho < 1.6$. In this light, it is interesting to examine a density ratio profile for Dive 1, which had an overall T-S stratification in the fingering sense. Figure 16 shows profiles of T, S, $R\rho$ and mixing intensity for Dive 1. A least squares fit of T to S over about 15 db was used to compute $R\rho$. $R\rho$ is greater than two in the upper water and fingers may be active on the interfaces associated with irregular steppiness in the upper 180 db, but since the steps lack the distinctive staircase appearance found in double-diffusive layering (Schmitt, 1981), and finger growth rates would be relatively slow, we suspect that this finestructure is due to internal wave straining with salt fingers playing only a parasitic role. However, deeper in the water column, at about 380 db, there appears to be an instance of mixing activity being associated with a minimum in $R\rho$, as well as finestructure steps. This is the sort of correlation expected from the model of Schmitt (1981) in which fingers only become strong when the density ratio drops sufficiently close to one. The density ratio also drops below 1.5 at about 230 db, but apparently the gradients are so weak in this region that any salt fingers would be too weak to be observed by SCIMP. We should also remark that the finescale variability in $R\rho$ seen in this central water station does not contradict the prediction of the Schmitt (1981) model that large-scale mean profiles should tend toward a constant $R\rho$; rather the coincidence of mixing activity with low $R\rho$ illustrates the mechanism in operation.

We can examine the data of the several dives for correlations of the mixing

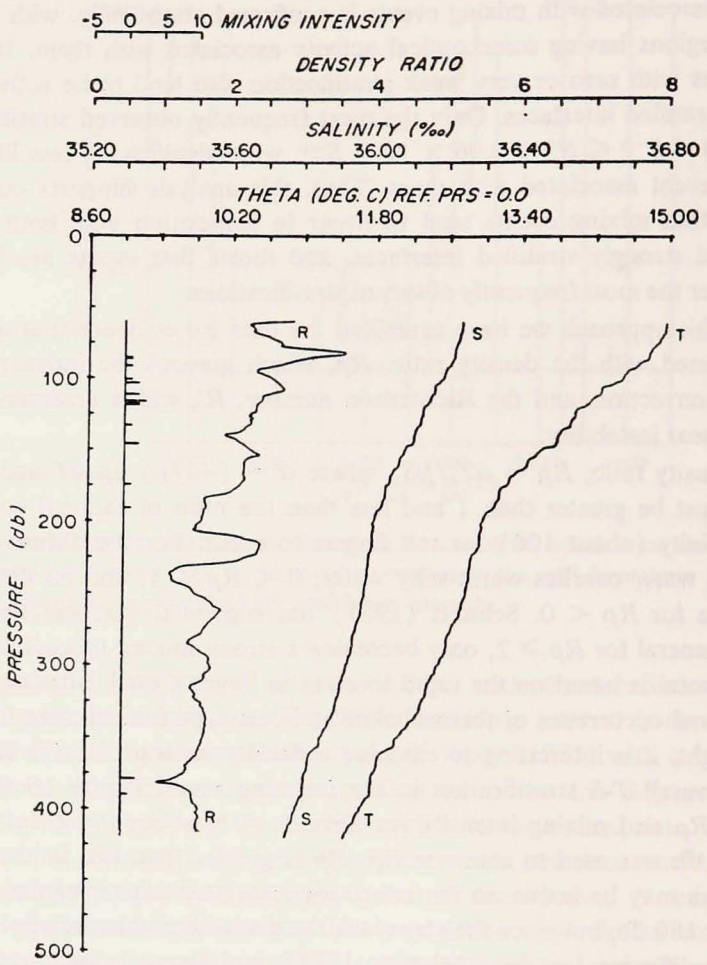

Figure 16. Profiles of θ, S, density ratio ($R\rho$) and mixing intensity for Dive 1.

activity with $R\rho$ near one, with the statistical method demonstrated with N^2. Figures 17a,b,c,d, show the probability of observing a mixing event as a function of $R\rho$ for each of the four dives. The dirth of mixing activity in Dive 1 precludes our ability to find statistically significant deviations from the null hypothesis (Fig. 17a); there being too few events to render the peaks toward high $R\rho$ significant. However, Dives 2 and 3 (Figs. 17b and 17c) do show a significantly higher probability of observing mixing activity when $R\rho$ is near one, a significantly lower probability for $R\rho$ away from one. Dive 4 (Fig. 17d) shows a pattern similar to Dives 2 and 3 but with a less significant peak, probably due to the degraded optical signal on this dive. Figure 17e shows the composite statistics for all four dives with a smaller bin size in $R\rho$. Clearly there is a significantly higher likelihood of seeing a mixing

event for $0.5 < R\rho < 1.25$ and a significantly lower probability of seeing activity for $R\rho < 0.25$ and $R\rho > 2.0$. This is consistent with theory, which predicts that double-diffusion will be strongest when $R\rho$ is close to one and suggests that a significant fraction of the microstructure observed in these dives is due to salt fingering and diffusive interfaces.

We note that the percentages of mixing observed in these dives are generally below 50%. This appears to be due to the fact that many of the observations with $R\rho$ near one had relatively weak gradients so that any microstructure present could be below the detection threshold of the SCIMP optical system. We can check for a dependence on the gradient strength as well as $R\rho$ by examining the probability of observing a mixing event as a function of both $R\rho$ and N^2. Such a plot is given in Figure 18 with data from all four dives included; contours of 80%, 50%, and 20% are indicated. The figure clearly shows that strong interfaces with $R\rho$ near one are virtually certain to show activity, while weakly stratified regions or strongly stratified regions with $R\rho < 0$, are much less likely to display optical microstructure. We also see that unstably stratified and very weakly stratified regions, especially with $R\rho$ near one, are more likely to be active. This indicates that mixing tends to occur at either sheets or layers and tends to avoid regions having an intermediate stratification, unless $R\rho$ is very close to one. As will be discussed later, a large fraction of the observed mixing was associated with the "$R\rho$ near one" pattern.

Another parameter which bears on the mixing of a stratified fluid is the Richardson number, $Ri = N^2/S^2$. As mentioned earlier, SCIMP does not resolve all of the shear, so we are most likely to overestimate the Richardson number. However, since most mixing events have a rather small vertical scale (< 1 m), and SCIMP does a fair job of resolving such scales, we expect there should be some correlation of mixing activity with low Ri, if shear instability plays any role in ocean mixing.

The probabilities of seeing a mixing event as a function of Richardson number for the four dives are shown in Figures 19a,b,c,d. Dive 1 had too few events to show any trends. Dives 2 and 3 show a significant correlation of mixing events with low Richardson number; a significant decrease in correlation at high Richardson numbers. Dive 4 shows similar trends but with a lower significance, perhaps because of the misaligned optics.

Composite statistics for the last three dives (from the front) are shown in Figure 19e. A significantly higher percentage of mixing was observed for Richardson numbers less than two, a significantly lower percentage of mixing for Ri greater than 5. No particular increase in activity is found at $Ri < \frac{1}{4}$; the theoretical maximum limit for shear instability to occur; but rather a general increase for $Ri < 2$ is observed. This is probably due to two effects: (1) SCIMP tends to overestimate Ri and (2) it is quite likely that some of the activity seen by SCIMP is

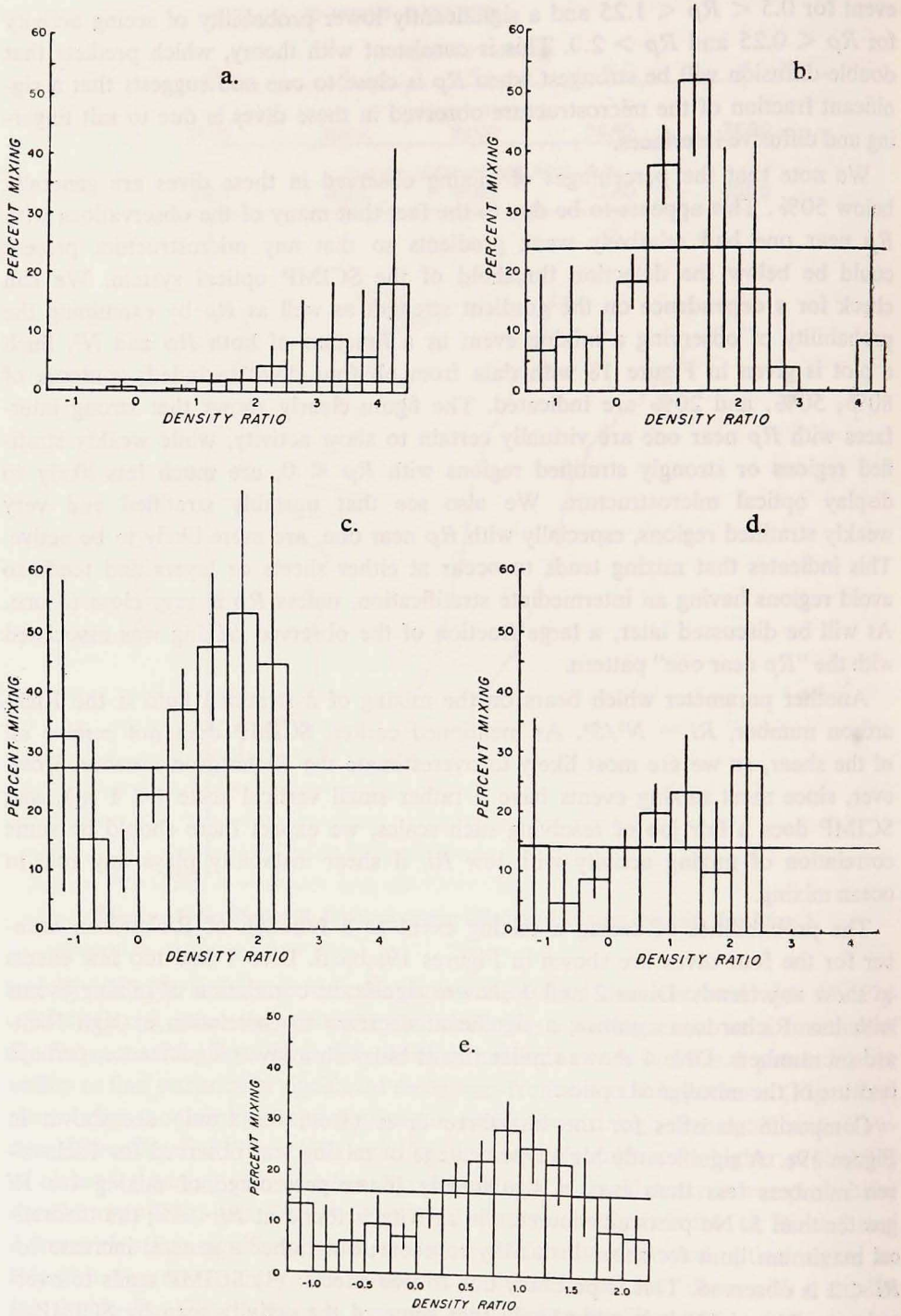

Figure 17. The probability of observing mixing activity for different values of $R\rho$. The horizontal line represents the null hypothesis; the error bars are the 95% confidence intervals. (a) = Dive 1; (b) = Dive 2; (c) = Dive 3; (d) = Dive 4; (e) = all dives.

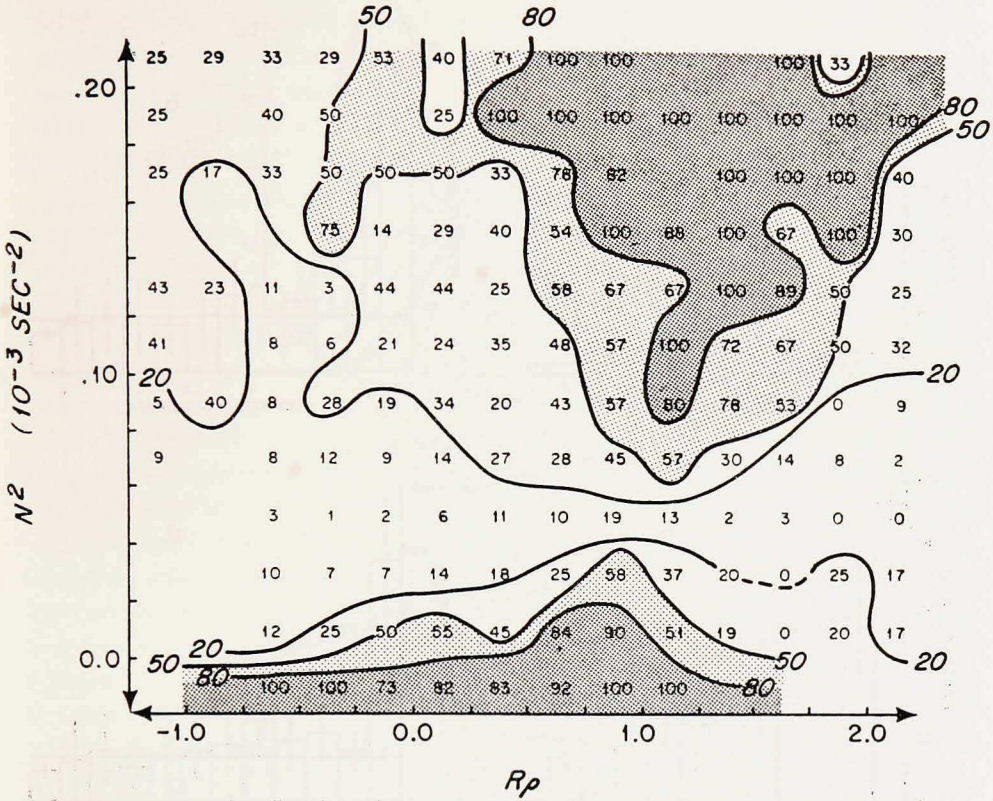

Figure 18. Contours of the probability of observing mixing activity as a function of N^2 and $R\rho$ for all dives.

caused by mixing events in which the velocity field has already decayed, so that the Richardson numbers are no longer low. We also do not see evidence of a distinct transition at $Ri = \frac{1}{4}$ in the overall incidence of Richardson number. A histogram of the percentage occurrence of Ri for the last three dives showed a slight peak for $Ri \cong 1$ with a very slow decrease with increasing Ri. About 1% of the observations had $Ri \leqslant 0$, about 2.5% had $0 < Ri \leqslant \frac{1}{4}$ and 12.5% had $\frac{1}{4} < Ri \leqslant 1.5$. However, there was no particular sharp transition at $Ri = \frac{1}{4}$ as has been suggested by Eriksen (1978) and the median Richardson number was 6.7, significantly higher than the value 1.5 we estimate from Eriksen's data. Both of these differences we ascribe to SCIMP's inability to resolve all of the shear.

However, despite this shortcoming, we have found distinct correlations of mixing activity with low Ri and have been able to use these correlations to classify the relative importance of shear instability and double-diffusion in causing the observed microstructure. Our approach is to examine the incidence of mixing as

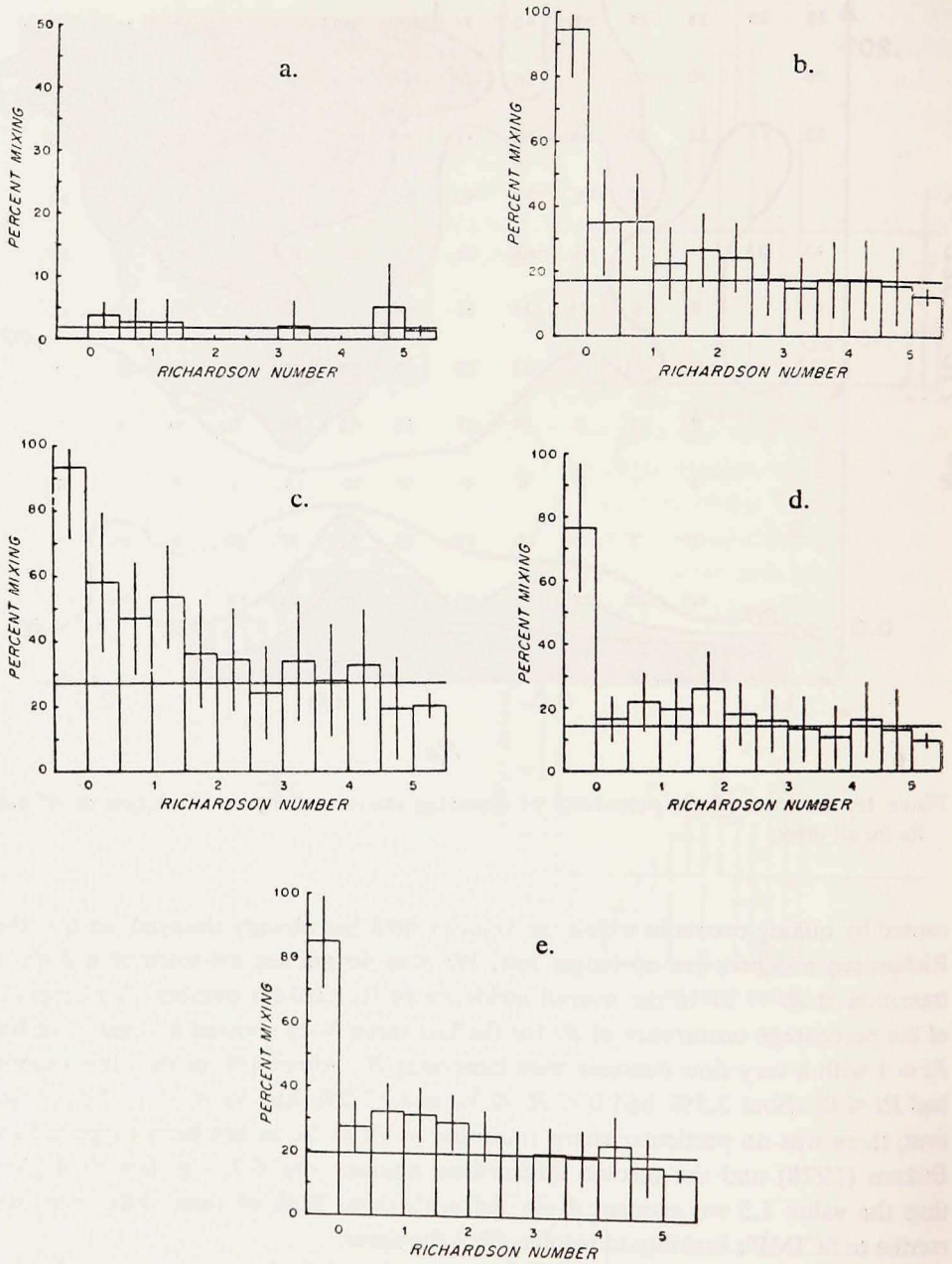

Figure 19. The probability of observing mixing activity for different values of the Richardson number. The horizontal line represents the null hypothesis; the error bars are the 95% confidence intervals. (a) = Dive 1; (b) = Dive 2; (c) = Dive 3; (d) = Dive 4; (e) = Dives 2,3,4.

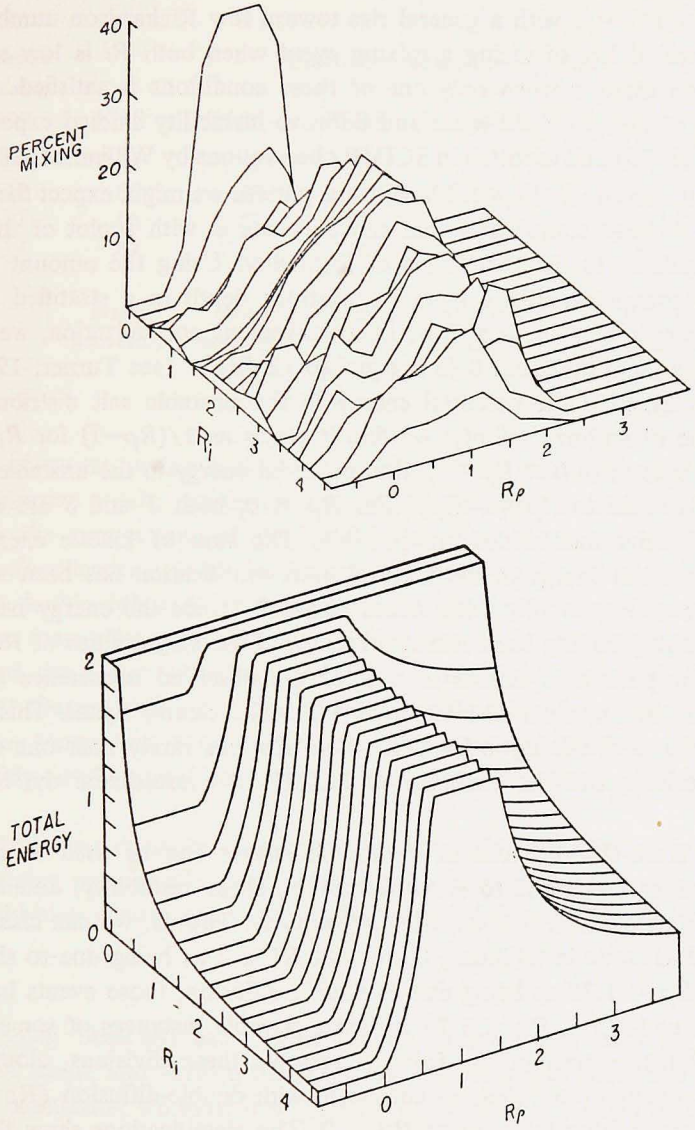

Figure 20. (a) The probability of observing a mixing event as a function of Richardson number and density ratio for all four dives. Limited smoothing over adjacent points has been applied and bins with few observations have been set to zero; (b) The sum of the kinetic and potential energy available for mixing as a function of Ri and $R\rho$. The amount of energy required to stir to uniformity has been used as the normalization.

a function of both Ri and $R\rho$. Perhaps the best way to visualize this data is in the form of a three-dimensional plot of the percent occurrence of mixing events in Ri and $R\rho$ space (Fig. 20a). The data clearly display a "double-diffusive ridge"

centered along $R\rho = 1$ with a general rise toward low Richardson number. There is a higher probability of seeing a mixing event when both Ri is low and $R\rho$ is near one, than there is when only one of these conditions is satisfied. This may be indicative of the combined shear and diffusive instability studied experimentally by Shirtcliffe (1973) and reported in SCIMP observations by Williams (1981).

It is helpful to compare Figure 20a with the pattern we might expect theoretically. Perhaps the simplest comparison that can be made is with a plot of the amount of energy available to the two forms of instability. Using the amount of energy necessary to completely mix a layer of arbitrary depth in a stratified fluid with constant gradients of T, S, ρ and U, as a convenient normalization, we find that the kinetic energy in the shear field is equal to $(2\ Ri)^{-1}$ (see Turner, 1981). One can similarly examine the potential energy in the unstable salt distribution relative to a state of uniform salinity; we find it scales as $1/(R\rho-1)$ for $R\rho > 1$. In the diffusive case, with $0 < R\rho < 1$, the potential energy in the unstable temperature profile is equal to $R\rho/(1-R\rho)$. For $R\rho < 0$, both T and S are stable and no double-diffusive instabilities are possible. The sum of kinetic energy in the shear and potential energy in the thermohaline stratification has been mapped in Ri, $R\rho$ space in Figure 20b, with values above 2 (twice the energy necessary to stir to uniformity) having been truncated to avoid the singularities at $Ri = 0$ and $R\rho = 1$. The pattern is similar to that of the observed occurrence of mixing, though the distinct correlation along $R\rho = 1$ is the clearer signal. This is due to the low incidence of mixing in Dive 1, where $R\rho$ was rarely near one due to the lack of intrusions, and the tendency of SCIMP to overestimate the Richardson number.

The data from the divisions in Ri and $R\rho$ space can be used to classify the mixing events as being due to static instability, shear instability, double-diffusion or combinations of shear and diffusive instabilities. That is, we can classify events with $N^2 < 0$ as static instabilities, those with $Ri < 2$ as being due to shear, those with $.25 < R\rho < 1.75$ as being due to double-diffusion, those events having both $0 < Ri < 2$ and $.25 < R\rho < 1.75$ as being possible instances of some combined shear and diffusive mechanism. Table 2 presents these divisions, along with the fractions of mixing events that are consistent with double-diffusion ($R\rho > 0$) and those that have neither low Ri nor $R\rho > 0$. The classifications show that Dive 1 is markedly different from the frontal dives, for while nearly all the events are consistent with double-diffusion, only 31% fall within the $.25 < R\rho < 1.75$ range where double-diffusion must be considered likely. However, 55% of the events are associated with low Richardson numbers, suggesting that shear instability was the more common event in the weakly mixing mid-gyre where less than 2% of the frames showed activity. The frontal dives, however, clearly show a dominance of double-diffusive processes; with 59 to 85% of the events falling in the $.25 < R\rho < 1.75$ range while only 27 to 35% have low Richardson numbers. Even if

Table 2.

Dive	Incidence of mixing events	Fraction of mixing events with: $N^2<0$	$0<Ri<2$	$0<R\rho$	$.25<R\rho<1.75$	$0<Ri<2$ $.25<R\rho<1.75$	$Ri>2$ $R\rho<0$
1	<0.02	0	.55	.97	.31	.17	0
2	0.17	.04	.27	.94	.85	.23	.06
3	0.27	.02	.29	.87	.72	.21	.07
4	0.14	.07	.35	.78	.59	.22	.07
Mechanism		static instability	shear instability	double-diffusion possible	double-diffusion likely	both shear and double-diffusion likely	other

the 21-23% of events having both low Ri and $R\rho$ near one, are subtracted from the double-diffusive totals, double-diffusion still accounts for half of the mixing events. Since the proportions of double-diffusion and shear are similar to the mixing type classifications given to the optical data, we feel that this is strong evidence that double-diffusion is the main reason for the increased microstructure activity in the front. We note that there is a remarkable similarity between the proportions of shear and diffusive instabilities reported here, and the classifications made by Gargett (1976). From towed microstructure data in a region with intrusions, she found that one-third of the mixing events could be classified as shear instabiltiy, while two-thirds of the events appeared to be double-diffusive in origin.

Thus, fairly strong evidence is accumulating that double-diffusion is a significant ocean mixing process wherever lateral intrusions provide sites with "$R\rho$ near one" that yield high growth rates for the finger and diffusive instabilities.

5. Discussion

Having directly observed salt fingers acting on intrusions with an apparent cross-isopycnal slope, and verified the statistical correlation of microstructure with $R\rho$ near one conditions, we must now attempt to estimate the effect of this small-scale mixing on the larger-scale hydrography. Joyce (1977) provided a framework for estimating the amount of lateral mixing caused by the interleaving of two different water types, finding that the large-scale lateral diffusivity (A_h) is given by:

$$A_h = A_z \frac{\langle T_z^2 \rangle}{T_y^2}$$

where A_z is the vertical diffusivity acting across the boundaries of the intrusions, $\langle T_z^2 \rangle$ is the variance of the vertical temperature gradient and T_y is the mean lat-

eral temperature gradient. The temperature gradients can be estimated from CTD casts; the main unknown in applying the Joyce model is the value of the vertical diffusivity. An approach which has been used with thermohaline staircase observations is to apply the flux laws derived from laboratory experiments on double-diffusion to the observed temperature and salinity steps (Lambert and Sturges, 1976; Middleton and Foster, 1980; Schmitt, 1981). Dividing these fluxes by the mean gradients then gives an estimate of the effective vertical diffusivity. Some direct evidence that such a procedure may be valid comes from microstructure tow data reported by Gargett and Schmitt (1982). Narrow band temperature microstructure from a horizontal tow through a warm-salty over cold-fresh interface was found to have a spectral shape similar to that predicted for salt fingers, and a total temperature variance close to what would be expected from the application of the laboratory flux laws. Thus, we have adopted the same approach, using the steps in salinity in the expanded profile of the salt fingering region in Dive 3. The total salinity change is about 0.16‰ at the bottom of the intrusion. However, Figure 12 clearly shows that this transition occurs not at one sharp interface but across several smaller steps, 0.02 to .04‰ in magnitude. The salt density flux due to fingers has been given by Schmitt (1979b) as $\beta F_s = C \cdot (g\ K_t)^{1/3}\ (\beta \Delta S)^{4/3}$ where C is a coefficient of about 0.1 for $R\rho < 2$. This coefficient may increase rapidly as $R\rho \to 1$, but the difficulties of measuring the high fluxes obtained when $R\rho$ is near one leaves any extrapolation uncertain; 0.1 should be regarded as a minimum for C. Taking $\Delta S = 0.03$‰, $\beta = .788 \times 10^{-3}$/‰, we get a salt density flux of 7.5×10^{-8} cm/s. We estimate the mean vertical salt gradient to be 7.3×10^{-5}‰/cm (= 0.16‰/22 m where 22 m is the approximate distance between the centers of the mixed layers above and below the finger region). Dividing the flux by the density gradient due to salt (βS_z) yields an apparent salt diffusivity of 1.3 cm²/s. This should be considered as only an order of magnitude estimate because of the uncertainties inherent to such a calculation. A value of 1 cm/s has been used by Joyce *et al.* (1978) and Georgi (1981). It is somewhat lower than the estimates obtained from the thermohaline staircases (i.e., ~ 10 cm²/s) (Schmitt, 1981) largely because the mean gradient must be defined over a smaller vertical distance within the intrusions as compared to the staircases, which often extend for hundreds of meters.

The heat flux associated with the fingers is less than the salt flux, because the thermal diffusion between adjacent fingers short circuits the vertical heat advection by the fingers. Using a heat/salt flux ratio (γ) of 0.7 as suggested by the laboratory data, a thermal buoyancy flux of 5.25×10^{-8} cm/s is obtained. With the mean vertical temperature gradient of about 6×10^{-4}°C/cm, and $\alpha \cong -.125 \times 10^{-3}$/°C, the thermal eddy diffusivity can be estimated as 0.7 cm²/s.

If we can take these numbers as being applicable to the other intrusions in the nearby CTD profiles from the first Tow-yo, we can then apply the Joyce model.

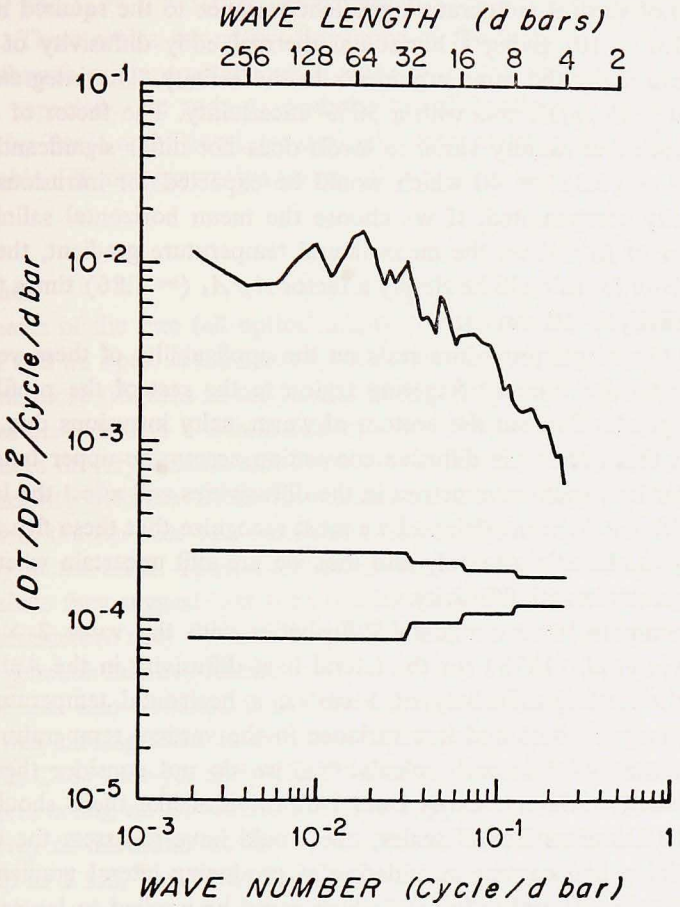

Figure 21. Ensemble averaged temperature gradient spectrum from the 13 downcasts of Tow-yo 1, for the pressure interval 100 356 db. The estimated 95% confidence intervals are shown in the lower portion of the figure.

The variance in the vertical temperature gradient can be estimated by integrating the vertical temperature gradient spectrum over the appropriate wavenumber band. Figure 21 is the ensemble averaged temperature gradient spectrum from the 13 downcasts of Tow-yo 1 for the pressure interval of 100 to 356 db. If we integrate the variance over the wavelengths of 128 to 16 m, (since this is close to the scale on which we estimated the vertical eddy diffusivities), we obtain 7.6×10^{-4} $(°C/m)^2$ with a standard deviation of about 30%. Our uncertainty in choosing a mean lateral gradient is greater; from the contoured temperature profiles (Fig. 9), we might choose $1°C/10 \text{ km} = 1 \times 10^{-4}°C/m$ as being representative of the gradient along isopycnals in this region. Thus, $(T_y)^2 \simeq 10^{-8}$ $(°C/m)^2$

and the ratio of vertical temperature gradient variance to the squared mean lateral gradient is 7.6×10^4 giving a horizontal thermal eddy diffusivity of 5.3×10^4 cm^2/s. We can apply the same arguments to the salinity. The integrated variance is 0.16×10^{-4} (‰/m)^2, also with a 30% uncertainty. The factor of 50 between the temperature and salinity variance levels does not differ significantly from the ratio $(\beta/\alpha)^2 \sim (6.3)^2 = 40$ which would be expected for intrusions which are entirely density compensated. If we choose the mean horizontal salinity gradient to be a factor of β/α times the mean lateral temperature gradient, then the horizontal diffusivity for salt will be simply a factor A_s/A_t ($= 1.86$) times the horizontal heat diffusivity, $\sim 10^5$ cm^2/s.

However, this whole procedure rests on the applicability of these vertical diffusivities estimated for one salt fingering region to the rest of the profiles. In fact, we expect a greater flux out the bottom of warm, salty intrusions due to fingering than the flux that occurs via diffusive convection across the upper boundary. It is not at all clear how such asymmetries in the diffusivities will affect the lateral fluxes calculated with the Joyce model, and we must recognize that these figures represent order of magnitude estimates only and that we are still uncertain whether heat or salt has the greater lateral diffusivity.

We can compare these horizontal diffusivities with the value 2×10^5 cm^2/s given by Joyce *et al.* (1978) for the lateral heat diffusivity in the Antarctic Polar Front using a vertical diffusivity of 1 cm^2/s, a horizontal temperature gradient one-third as large as ours and less variance in the vertical temperature gradients. Given the uncertainties in such calculations, we do not consider these estimates to be significantly different. Cross frontal diffusivities like these should be applicable to 5-10 km cross frontal scales; one would have to assess the effectiveness of eddy straining and current meandering at producing lateral gradients on these scales to estimate a lateral diffusivity which could be applied to larger scales.

The spectra, Figure 21, are also useful for estimating the dominant vertical scales of the intrusions. There is a broad peak in the gradient spectrum for wavelengths between 20 and 100 m. Toole and Georgi (1981) have considered the problem of the generation of double-diffusive intrusions; extending the original analysis of Stern (1967) to include the effects of a vertical eddy viscosity. They find that the fastest growing intrusion has a vertical scale given by:

$$L_z = \frac{2\pi}{D} \frac{N^{1/2} (A_s A_v)^{1/4}}{(1-\gamma)^{1/2} (g\beta S_x)^{1/2}}$$

where A_v is the eddy diffusivity for momentum and other variables have their usual definition. The factor D can be taken from Figure 7 of Toole and Georgi. In the parameter range appropriate to our data we evaluate D as 0.48 if $A_v = A_s$ and $D = 0.67$ if $A_v = 0.1\ A_s$. Since there exists no data bearing on the relationship between momentum and salt eddy diffusivities for salt fingers we can only make length scale estimates based on these two cases. With $A_v = A_s = 1.3$ cm^2/s, $N = 2$

cph, $\gamma = 0.7$ and $S_x = 1 \times 10^{-5}‰/\text{m}$ we obtain $L_z = 40$ m, while if $A_v = 0.1\ A_s$, $L_z = 19$ m. These scales are within the range of the broad spectral peak seen in Figure 21, though perhaps on the small side. Given the uncertainties in all of the parameters, especially A_v and A_s, and the broad bandedness of the growthrate peak found by Toole and Georgi, we can only claim consistency of these intrusions with the double-diffusive generation theory.

6. Conclusions

Deployments of the free fall optical microstructure profiler (SCIMP) in a mid-gyre region and an open ocean front have shown that mixing events are an order of magnitude more frequent in the frontal interleaving zone than in mid-gyre. The frontal dives also showed a dominance of vertically-oriented microstructure, with several patches of very distinct salt fingers being observed. Significant correlations of mixing activity with low Richardson numbers and density ratios near one were obtained, with the $R\rho$ near one correlation accounting for most of the microstructure activity at the front. These correlations may be the most important result of this study since they suggest that high quality profiles of temperature, salinity and velocity finestructure may be used to predict a significant fraction of the mixing events that generate microstructure.

Evidence was also obtained that double-diffusion acting on the boundaries of intrusions was causing them to propagate across density surfaces. By performing simultaneous CTD Tow-yos and SCIMP dives we were able to obtain photographs of salt fingers acting on an intrusion with an apparent cross-isopycnal slope. Our limited survey of intrusions at the front revealed that they had lateral coherence scales of up to 5 km, and vertical scales of 5 to 50 m, which are consistent with the double-diffusive generation theory of Stern (1967) and Toole and Georgi (1981). While we cannot prove that double-diffusion is driving the intrusions, we do feel that the evidence that double-diffusion is acting on the intrusions is irrefutable.

By applying the laboratory flux laws to observed temperature and salinity finestructure we have estimated an effective vertical eddy diffusivity due to the salt fingers of about 1 cm²/s. Applying this to the Joyce (1977) model of lateral mixing, yields a lateral diffusivity of .5 to 1×10^5 cm²/s, which should be applicable to cross-frontal water mass transitions with scales of order 5 km. We note that the factor of 10^5 between the vertical and horizontal diffusivities is two orders of magnitude larger than the factor of 10^3 estimated for horizontal shear dispersion due to internal waves by Young *et al.* (1982). This suggests that lateral mixing will be particularly strong where T and S gradients exist along density surfaces. One would have to determine the effectiveness of the mesoscale eddy processes at producing thermohaline gradients along isopycnal surfaces on 1-5 km scales to

determine the importance of the interleaving mechanism to the general circulation on scales of 10^3 km.

Acknowledgments. The authors would like to thank Dr. Albert J. Williams III for generously allowing us to use SCIMP and Mr. Alfred Morton for ably assisting us at sea. Drs. Dave Evans and Peter Hendricks provided software and Dr. Ted Green supplied some excellent satellite imagery. Both of us are indebted to Valentine Worthington who, while pursuing his own understanding of the large-scale circulation, was always supportive of our interest in small-scale oceanic processes. We also acknowledge the support of the Office of Naval Research, Contract Number N00014-79-C-0071, NR 083-004. This is contribution number 4969 from the Woods Hole Oceanographic Institution.

REFERENCES

Bray, N. A. and N. P. Fofonoff. 1981. Available potential energy for MODE eddies. J. Phys. Oceanogr., *11*, 30–47.

Eriksen, C. C. 1978. Measurements and models of finestructure, internal gravity waves, and wave breaking in the deep ocean. J. Geophys. Res., *83*, 2989–3009.

Evans, D. L., H. T. Rossby, M. Mork and T. Gytre. 1979. YVETTE—a free-fall shear profiler. Deep-Sea Res., *26*, 703–718.

Gargett, A. E. 1976. An investigation of oceanic turbulence with respect to fine structure. J. Phys. Oceanogr., *6*, 139–156.

Gargett, A. E., P. J. Hendricks, T. B. Sanford, T. R. Osborn and A. J. Williams III. 1981. A composite spectrum of shear in the upper ocean. J. Phys. Oceanogr., *7*, 436–454.

Gargett, A. E. and R. W. Schmitt. 1982. Observations of salt fingers in the central waters of the eastern North Pacific. J. Geophys. Res., (in press).

Georgi, D .T. 1981. On the relationship between the large-scale property variations and finestructure in the circumpolar deep water. J. Geophys. Res., *86*, 6556–6566.

Georgi, D. T. and R. W. Schmitt. 1982. Fine- and microstructure observations on a hydrographic section from the Azores to the Flemish Cap. J. Phys. Oceanogr., (submitted).

Gregg, M. C. 1977. Variations in the intensity of small-scale mixing in the main thermocline. J. Phys. Oceanogr., *7*, 436–454.

—— 1980. The three-dimensional mapping of a small thermohaline intrusion. J. Phys. Oceanogr., *10*, 1468–1492.

Hendricks, P. J. and G. Rodenbusch. 1981. Interpretation of velocity profiles measured by freely sinking probes. Deep-Sea Res., *28*, 1199–1213.

Hollander, M. and D. A. Wolfe. 1973. Nonparametric Statistical Methods, J. Wiley and Sons, New York, 23.

Horne, E. P. W. 1978. Interleaving at the subsurface front in the Slope Water off Nova Scotia. J. Geophys. Res., *83*, 3659–3671.

Johnson, C. L., C. S. Cox and B. Gallagher. 1978. The separation of wave-induced and intrusive oceanic finestructure. J. Phys. Oceanogr., *8*, 846–860.

Joyce, T. M. 1977. A note on the lateral mixing of water masses. J. Phys. Oceanogr., *7*, 626–629.

Joyce, T. M., W. Zenk and J. M. Toole. 1978. The anatomy of the Antarctic Polar Front in the Drake Passage. J. Geophys. Res., *83*, 6093–6113.

Lambert, R. A. and W. E. Sturges. 1976. A thermohaline staircase and vertical mixing in the thermocline. Deep-Sea Res., *23*, 211–222.

Linden, P. F. 1974. Salt fingers in a steady shear flow. Geophys. Fluid Dyn., *6*, 1–27.

—— 1978. The formation of banded salt finger structure. J. Geophys. Res., *83*, 2902–2912.

Middleton, J. H. and T. P. Foster. 1980. Finestructure measurements in a temperature-compensated halocline. J. Geophys. Res., *85*, 1107–1122.

Robinson, M. K., R. A. Bauer and E. H. Schroeder. 1979. Atlas of North Atlantic-Indian Ocean Monthly Mean Temperatures and Mean Salinities of the Surface Layer. Dept. of the Navy, Washington, D.C. (Figure 44).

Ruddick, B. R. and J. S. Turner. 1979. The vertical length scale of double-diffusive intrusions. Deep-Sea Res., *26*, 903–913.

Schmitt, R. W. 1979a. The growth rate of super-critical salt fingers. Deep-Sea Res., *26A*, 23–40.

—— 1979b. Flux measurements on salt fingers at an interface. J. Mar. Res., *37*, 419–435.

—— 1981. Form of the temperature-salinity relationship in the central water: evidence for double-diffusive mixing. J. Phys. Oceanogr., *11*, 1015–1026.

Shirtcliffe, T. G. L. 1973. The contribution of double-diffusive processes to the vertical fluxes of salt and heat, *in* Oceanography of the South Pacific, 1972, New Zealand Comm. for UNESCO, Wellington, New Zealand, 137–139.

Stern, M. E. 1960. The "salt fountain" and thermohaline convection. Tellus, *12*, 172–175.

—— 1967. Lateral mixing of water masses. Deep-Sea Res., *14*, 747–753.

Toole, J. M. and D. T. Georgi. 1981. On the dynamics and effects of double-diffusively driven intrusions. Prog. in Oceanogr., *10*, 123–145.

Turner, J. S. 1978. Double-diffusive intrusions into a density gradient. J. Geophys. Res., *83*, 2887–2901.

—— 1981. Small-scale mixing processes, *in* The Evolution of Physical Oceanography, MIT Press, Cambridge, Massachusetts, 246.

Williams, A. J. 1975. Images of ocean microstructure. Deep-Sea Res., *22*, 811–829.

—— 1981. The role of double-diffusion in a Gulf Stream frontal intrusion. J. Geophys. Res., *86*, 1917–1928.

Young, W. R., P. B. Rhines and C. J. R. Garrett. 1982. Shear flow dispersion, internal waves and horizontal mixing in the ocean. J. Phys. Oceanogr., (submitted).

Received: *3 September, 1981*; revised: *2 February, 1982.*